

Optimization of Tandem Solar cells by Deep Learning



By
Ayesha Razi

School of Chemical and Materials Engineering
National University of Sciences and Technology

2023

Optimization of Tandem Solar cells by Deep Learning



Name: Ayesha Razi

Reg. No.2019-MS-NSE07-320772

This thesis is submitted as a partial fulfillment of the requirements for the degree of

MS in Nanoscience and Material Engineering

Supervisor Name: Dr. Amna Safdar

**School of Chemical and Materials Engineering (SCME)
National University of Sciences and Technology (NUST)**

H-12 Islamabad, Pakistan

August, 2023



THESIS ACCEPTANCE CERTIFICATE

Certified that final copy of MS thesis written by Ms **Ayesha Razi** (Registration No 00000320772), of School of Chemical & Materials Engineering (SCME) has been vetted by undersigned, found complete in all respects as per NUST Statues/Regulations, is free of plagiarism, errors, and mistakes and is accepted as partial fulfillment for award of MS degree. It is further certified that necessary amendments as pointed out by GEC members of the scholar have also been incorporated in the said thesis.

Signature: _____

Name of Supervisor: Dr Amna Safdar

Date: 17/08/2023

Signature (HOD): _____

Date: 18/8/2023

Signature (Dean/Principal): AA

Date: 18-8-2023



Form TH-1
(Must be type written)

National University of Sciences & Technology (NUST)
MASTER'S THESIS WORK
Formulation of Guidance and Examination Committee (GEC)

Name: Ayesha Razi
Department: Materials Engineering
Credit Hour Completed: 24hrs

NUST Regn No: 320772
Specialization: Nanoscience and Engineering
CGPA: 3.69

Course Work Completed

S/No	Code	Title	Core/Elective	CH	Grade
1	MSE-854	Characterizations of Materials	Core	3	B
2	NSE-813	Essential of Nanoscience and Engineering	Core	3	A
3	NSE-845	Nanolithography and Device Fabrication	Elective	3	A
4	RM-898	Research Methodology	Core	2	Q
5	MSE-856	Nanomaterials and Processing	Core	3	A
6	NSE-847	Essentials of NEMS/ MEMS	Elective	3	A
7	MSE-862	Electronic and Magnetic Materials	Elective	3	B+
8	MSE-952	Materials for Biomedical Applications	Elective	3	A
9	NSE-842	Nano Materials for Energy Applications	Elective	3	B

Date: 2nd June 2021.

Thesis Committee

- Name: Dr. Amna Saffdar (Supervisor)
Department: Department of Materials Engineering
- Name: Dr. Rabia Irfan (Co-Supervisor)
Department: Department of Computing
- Name: Dr. Aftab Akram
Department: Department of Materials Engineering
- Name: Dr. Mohsin Saleem
Department: Department of Materials Engineering

Student's Signature:

Signature:

Signature:

Signature:

Signature:

Date: 28/6/2021

Signature of Head of Department:

APPROVAL

Date: 30.6.2021

Dean/Principal

Distribution

- 1x copy to Exam Branch, Main Office NUST
- 1x copy to PGP Dte, Main Office NUST
- 1x copy to Exam branch, respective institute

School of Chemical and Materials Engineering (SCME) Sector H-12, Islamabad



National University of Sciences & Technology (NUST)

FORM TH-4

MASTER'S THESIS WORK

We hereby recommend that the dissertation prepared under our supervision by

Regn No & Name: 00000320772 Ayesha Razl

Title: Optimization of Tandem Solar Cells by Deep Learning.

Presented on: 10 Aug 2023 at: 1400 hrs in SCME Seminar Hall

Be accepted in partial fulfillment of the requirements for the award of Masters of Science degree in Nanoscience & Engineering.

Guidance & Examination Committee Members

Name: Dr M. Aftab Akram

Signature: [Signature]

Name: Dr Mohsin Saleem

Signature: [Signature]

Name: Dr Rabia Irfan (Co-Supervisor)

Signature: [Signature]

Supervisor's Name: Dr Amna Safdar

Signature: [Signature]

Dated: 10-08-2023

[Signature]
Head of Department

Date 17-08-23

[Signature]
Dean/Principal

Date 17-8-23

School of Chemical & Materials Engineering (SCME)

Plagiarism Certificate (Turnitin Report)

This thesis has been checked for Plagiarism. Turnitin report endorsed by Supervisor is attached.



Signature of Student

Ayesha Razi

2019-MS-NSE07-320772



Signature of Supervisor

Dedicated to my exceptional husband and parents whose tremendous support and cooperation led me to this wonderful accomplishment

Acknowledgements

First and foremost, I extend my heartfelt appreciation to my husband, who has played an instrumental role as my mentor. I am deeply grateful for his unwavering support, encouragement, and guidance during my research journey, which has helped me evolve into a proficient research scientist. Additionally, I am immensely grateful to my beloved parents for nurturing and supporting me through every aspect of my life, starting from my earliest days when I was learning to walk.

I would also like to express special thanks to my supervisor Dr. Amna Safdar and co-supervisor Dr. Rabia Irfan for his help throughout my thesis and for Lithography and nano-mechanical device courses which he has taught me. I can safely say that I haven't learned any other engineering subject in such depth as the ones which he has taught.

I would also like to pay special thanks to my husband and research assistant of Dr Rabia from KGB lab for his tremendous support and cooperation. Each time I got stuck in something; he came up with the solution. Without his help I wouldn't have been able to complete my thesis. I appreciate his patience and guidance throughout the whole thesis.

I would also like to thank HEC for funding my research and evaluation committee and express my special thanks to GEC member Dr. Aftab and Dr. Mohsin for their help and availability.

Finally, I would like to express my gratitude to all the individuals who have rendered valuable assistance to my s

Abstract

This study explores the use of deep learning to predict the optimal optical design for the top cell in tandem solar cells, to maximize power conversion efficiency. The study also investigates the effects of metasurfaces on tandem solar cell architecture, including the use of active layers as metasurfaces. The study proposes three stacked layers of metasurfaces, each with a specific function. Computational techniques are developed to analyze the optical responses of metasurfaces, including using simulation tools and algorithms. The study uses Artificial Neural Networks (ANN) and 2D Convolutional Neural Networks (CNN) to analyze a dataset of 10,578 $\text{TiO}_2/\text{CH}_3\text{NH}_3\text{PBr}_3/\text{ZnO}$ metasurfaces. Nine different CNN models were used with different architectures to identify the best hyperparameters that give the low mean square error. The results show that CNN shows high prediction accuracy of resonator geometry aside from the training dataset. The CNN-based predictions were generated much faster, taking an average of 0.3 ± 0.05 seconds per prediction, whereas each FDTD simulation ($n=9$) took approximately 25 minutes hence, the CNN is 85 times faster than conventional solvers. The Deep SHapley Additive Explanations (SHAP) framework was used to gain insights into CNN's predictions and understand the behavior of complex nanophotonic devices. The designed metasurfaces were integrated into a typical reference tandem solar cell architecture, and the study concludes that the proposed metasurfaces can significantly enhance the efficiency of tandem solar cells. The active layer comprises of near 90% absorption of solar spectrum. The average absorption of the top cell increased in the UV-vis region (650-800nm) up to 93.4%. The bandwidth of absorption in the the Silicon bottom cell also increased which shows that metasurface transmits or scatters the unabsorbed NIR light to bottom cell. The estimated J_{sc} of the top and bottom cell is $19.5\text{mA}/\text{cm}^2$ and $20\text{mA}/\text{cm}^2$ respectively. The J_{sc} in the top cell increased by $2\text{mA}/\text{cm}^2$ by integrating optimized metasurface with the bottom cell. The recorded V_{oc} of the solar cell is 0.7397V . The total J_{sc} of $35.91\text{ mA}/\text{cm}^2$. The fill factor observed is 82.2%

Key Words: *Tandem solar cells, Metasurfaces, Deep Learning, Convolutional Neural Networks, Numerical modeling, and simulation*

Table of Contents

Acknowledgements	iii
Abstract.....	iii
Table of Contents	iii
List of Figures.....	iii
List of Tables	xiii
Chapter 1: Introduction	1
1.1 Background	1
1.2 Tandem Photovoltaics and Nanomaterials	2
1.2.1 Light Management.....	3
1.2.2 Metasurfaces.....	4
1.3 Optical Optimization	5
1.4 Problem Statement	6
1.5 Objectives.....	6
1.6 Significance and Contribution.....	7
1.7 Thesis Organization.....	7
Chapter 2: Literature Review	9
2.1. Review of Metasurfaces	9
2.2. Review of Deep Learning in Optical Optimization of TSC.....	11
2.3. Critical Analysis.....	12
Chapter 3: Methodology.....	13
3.1. Research Design.....	13
3.2. Building Dataset.....	14
3.3. Dataset Pre-processing and Splitting	15

3.4.	CNN Architecture and Forward Propagation.....	15
3.5.	Inverse Design (Opening CNN Black Box).....	16
3.6.	Integration of Metasurface with Solar cell.....	17
3.7.	Software, Equipment, and Tools Details.....	17
Chapter 4: Analytical Expressions and Numerical Modelling for Simulations.....		18
4.1.	Mathematical Expressions for Simulations.....	18
4.1.1.	Time-averaged Instantaneous Poynting Vector.....	18
4.1.2.	Divergence of Poynting Vector and Absorption per unit Volume Calculations	19
4.2.	Material Properties	20
4.3.	Metasurface Simulation Set Up.....	21
4.4.	Solar Cell Simulation Set Up.....	22
Chapter 5: Arithmetic of CNN		25
5.1.	2D-CNN Architecture	25
5.1.1.	Input Layer	25
5.1.2.	Discrete Convolution.....	26
5.1.3.	Kernel	27
5.1.4.	Strides and Padding	29
5.1.5.	Pooling Layer	31
5.1.6.	Fully Connected Layer	31
5.2.	Model Details and Learnable Parameters.....	32
5.3.	Black Box Opening and Model Prediction	33
Chapter 6: Results and Discussion		35
6.1.	FTDT Results Based on Resonator Shape	35
6.2.	FTDT Results Based on Resonator Size	36
6.3.	CNN- Forward Propagation Results	37

6.4.	Prediction Results.....	38
6.5.	DeepShap Results.....	39
6.5.1.	SHAP Explanations:.....	39
6.5.2.	SHAP Cross-arm validation	40
6.6.	Solar Cells Absorption Result	44
6.7.	Generation Rate and External Quantum Efficiency	46
	Conclusion.....	50
	Prospects	50
	Appendix.....	57

List of Figures

Figure 1.1: Shockley Queisser Limit of Solar cells [68]	2
Figure 1.2: Si-perovskite TSC absorbs high and low-energy photons	3
Figure 1.3: Classification of Optical Optimization technique	5
Figure 3.1: Methodology Steps and Research Design	13
Figure 3.2: Metasurface Design (Left) with the 3D view and xz view (Right).....	14
Figure 3.3: Interface of ANSYS FDTD software (Left) with the 2D view xy and and xz view of metasurface 3D perspective view (Right).....	15
Figure 3.4: Specs of Google Collab (Left) and PC used for training Dataset (Right).....	16
Figure 3.5: Reconstructed image validated top contributing SHAP values	16
Figure 3.6: Top and Bottom cell def file of TSC in SCAPS-1D	17
Figure 4.1: Energy band diagram of Materials used in Perovskite Solar Cells [61]	20
Figure 4.2: Refractive index of perovskite, zinc monoxide and titanium dioxide at wavelength (400nm-1200nm)	21
Figure 4.3: Schematic representation of the 2T-Si/perovskite TSC	23
Figure 5.1: Example of a discrete convolution containing a single input and output feature map ($n = m = 1$) for 2D-convolution $N = 2, i_1 = i_2 = 7, k_1 = k_2 = 3$	27
Figure 5.2: Layouts of the 2D-kernels used in the CNN models.....	28
Figure 5.3: Receptive fields in feature map and Depth column	28
Figure 5.4: a) showing generalized strides where kernel takes 2 steps to give output size 3×3 b) an alternative way of sampling where kernel slides 1 step and translated to 2×2 output	30
Figure 5.5: showing half padding convolution of a 3×3 filter over a 5×5 input (i.e., $i = 5, k = 3, s = 1$ and $p = 1$)	30
Figure 5.6: showing full padding convolution of a 3×3 filter over a 7×7 input (i.e., $i = 5, k = 3, s = 1$ and $p = 2$)	30
Figure 5.7: Features maps in fully connected layers	32
Figure 6.1: Absorption spectrum of resonator w.r.t different shapes	35
Figure 6.2: Absorption spectrum of resonator w.r.t different sizes	36
Figure 6.3: Training Graphs showing a) CNN Model-9 Training and Validation Loss b) CNN Model-9 Training and Validation Accuracy	38

Figure 6.4: CNN Prediction and FDTD simulation of the 9-different resonator of the training dataset	39
Figure 6.5: SHAP CNN Explanations of metasurfaces (L1=2200nm, L2=300nm) Predictions at increasing wavelengths a) Window resonator b) Cross resonator c) L-arm resonator	40
Figure 6.6: SHAP CNN Validation at 450-800nm of a) L1=5200nm, L2=300nm b) L1 6800nm, L2= 500nm c) 8800nm, L2=700nm.....	40
Figure 6.7: SHAP CNN Validation a) Absorption peaks of window and cross resonator at L1=2200nm b) SHAP explanations of the resonators at wavelength 450-800nm c), d) SHAP explanation of the validated cross-window base image at 600-800nm	41
Figure 6.8: Average SHAP validation values of SHAP explanation a) 450nm b) 600nm c) 700nm d) 800nm.....	42
Figure 6.9: Resonance Profile of SHAP Validated Structures a) 450nm b) 600nm c) 700nm d) 800nm	43
Figure 6.10: Electric field Profile of SHAP Validated Structures a) 450nm b) 600nm c) 700nm d) 800nm	43
Figure 6.11: Optical absorption in 2T-perovskite/Si TSC (a) reference configuration without metasurface (b) configuration with integrated metasurface top cell.....	45
Figure 6.12: Optical absorption in 2T- perovskite/Si TSC (integrated metasurface) with reference to the AM 1.5 irradiance spectrum.....	46
Figure 6.13: Carrier Generation rate profile in 2T- perovskite/Si TSC (integrated metasurface)	46
Figure 6.14: EQE in 2T- perovskite/Si TSC (integrated metasurface).....	47

List of Tables

Table 2-1: Learning-based Methods for TSC Optimization	12
Table 3-1: Simulation Source, Unit cell dimension and Mesh setting.....	14
Table 3-2: Details about Equipment/ Software	17
Table 4-1: Material Properties used for Simulations	21
Table 4-2: 2D images of metasurface unit cell shapes and their design parameters	22
Table 4-3: Properties of materials used in TSC simulations.....	23
Table 5-1: Layers, Parameters of trained CNN architectures	34
Table 6-1: Outcomes of trained CNN with the associated RMSE values, validation accuracy, and training time	37
Table 6-2: Comparison of the state-of-the-art Metasurface with recent studies and findings.....	47

Chapter 1:

Introduction

This dissertation is split into two parts. The first part focuses on the optical optimization of metasurfaces for light management in Tandem solar cells (TSC). The objective is to employ deep learning to predict the optimal optical design for the top cell, maximizing power conversion efficiency. The second part involves studying the effect of metasurfaces on solar cell architecture. By integrating the findings of the optical optimization section with experimental data, this research searches for the impact of metasurfaces on solar cell performance.

1.1 Background

The world has recently seen the applications of several renewable energy sources that have assisted in resolving the energy crisis. The high demand for fossil fuels, which are expensive, rare, and have significant environmental issues, has decreased as a result [1]. The five main types of renewable power are wind, solar power, geothermal, hydro, and bioenergy. They are all abundant in nature and are reliable, inexpensive, clean, and safe. Implementing these resources, however, poses some practical difficulties, including high maintenance costs, transmission costs, and the need for large devices for conversion of energy from one form to another. In addition, energy sources including hydropower, geothermal, tidal, and biomass can increase atmospheric pollution brought on by greenhouse gases. Therefore, it is imperative to create technologies and infrastructure that will enable the construction of renewable energy sources while lowering the usage of fossil fuels and other sources of energy that are not sustainable.

Photovoltaic (PV) technology is widely considered the most viable method to harness solar energy and meet the present and future needs for clean energy, while also minimizing carbon dioxide emissions. About 48% of the solar energy that reaches the Earth is visible, 44 percent is infrared spectrum and seven percent is ultraviolet. At the core of any PV technology lies the solar cell. Over the last 20 years, the field of PV technology has experienced remarkable progress, expanding from its niche applications to becoming a mainstream source of energy. The Silicon

(Si)-based single junction cells (SJs) have a dominant market share among the various types of solar power cells that are offered on the market.

These cells boast a power conversion efficiency (PCE) till 26.7%, making them an attractive option for various applications [2]. The current and voltage potential of solar cells are governed by bandgap. The bandgap is the gap between the electron affinity at the bottom of the band of conduction and the ionisation potential at the apex of valence band. A photon can only be absorbed if its energy is higher or equal that of the bandgap value by the semiconductor as shown in Figure 1.1. The solar spectrum comprises photons of a broad range of energy, mostly situated between 1 and 4 electron-volts (eV). Decreasing the bandgap of the absorbing semiconductor can help generate more current. However, the bandgap also restricts the voltage at which the current can be extracted. In practice, it is impossible to extract the current at a voltage higher than the bandgap. This limit is called Shockley Queisser Limit [3], [4]

The performance of SJC is constrained by several other factors, including the second law of thermodynamics, indirect bandgap, and low power yield. These cells can only absorb photons with energy greater than their bandgap, and even then, not all the energy can be converted into electrical energy due to recombination losses [5]. As a result, their overall efficiency is limited.

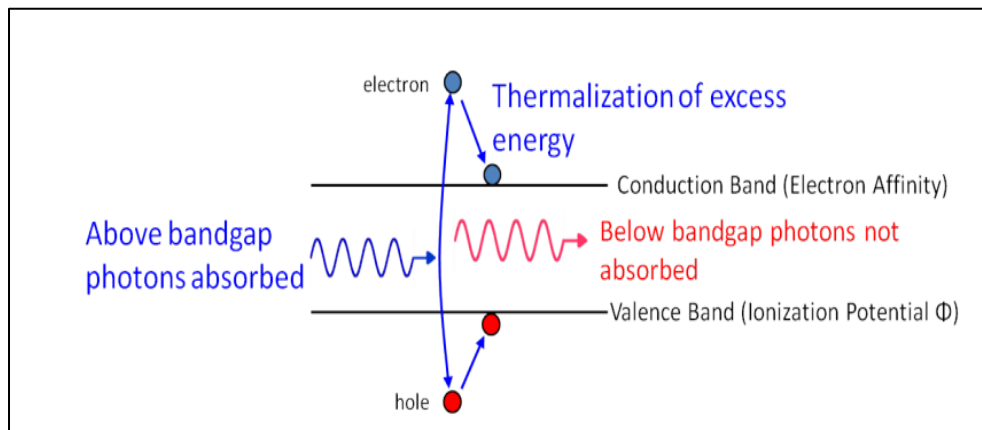


Figure 1.1: Shockley Queisser Limit of Solar cells [68]

1.2 Tandem Photovoltaics and Nanomaterials

In the 1980s, research into multi-junction solar cells (MJC) emerged as a potential replacement for SJs, and TSC are now seen as the next phase in solar cell development. TSCs are designed to absorb high and low-energy photons using wide-bandgap and low-bandgap active layers, respectively, thereby outperforming the Shockley Queisser Limit as shown in Figure 1.2.

TSCs are also cost-effective since Si can act as a substrate material. However, achieving efficient optical design in TSCs is a major challenge as advanced control over light management is required. The performance of TSCs is limited by reflective and parasitic losses, which ultimately decrease their efficiency and cause current mismatching.

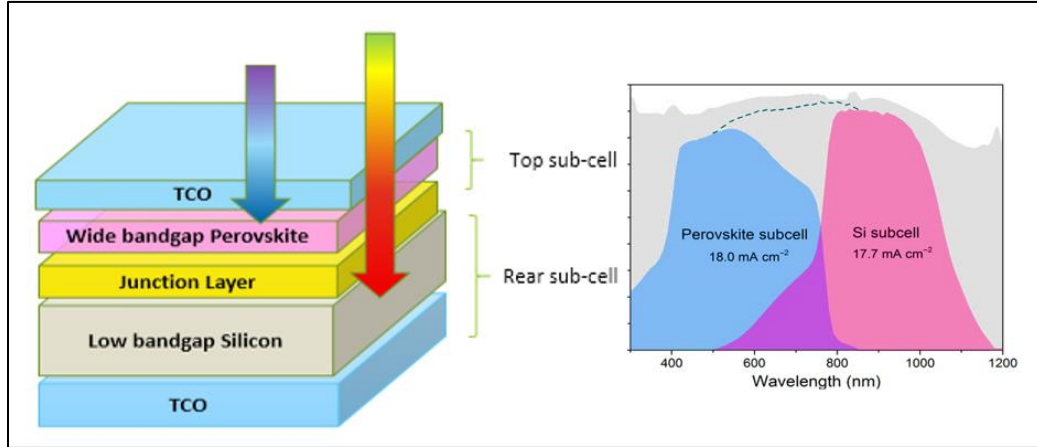


Figure 1.2: Si-perovskite TSC absorbs high and low-energy photons

The best combination for highly efficient double-junction Top cells in TSCs have a bandgap between 1.7 and 2 eV, and rear-end cells have a bandgap energy of 1.12 eV [6]. So, crystalline Si and perovskite are the best choices for the bottom and top cells, respectively, in tandem configuration [7]. The experimental PCE, on the other hand, is significantly lower than the theoretically calculated potential (i.e., 42-45%). With n^{++}/p^{++} tunnel junction, Mailoa *et al* [8] demonstrated a homojunction c-Si rear cell with a stable PCE-equipped perovskite the top cell of 13.8 percent. Wu *et al* [9] used a two terminal (2T)-mesoscopic perovskite top cell and homojunction Si cell to create a tandem device. Due to homojunction Si-sub-cell perovskite's high-temperature tolerance, mesoporous TiO_2 was used in tandems to reduce the Si subcell's optical losses and achieve a PCE of 22.5 percent. Another group used NiO as carrier transporting layer between the Si perovskite sub-cell and the perovskite upper cell 2T tandem, achieving a stable efficiency of 21.19 percent (Kim *et al.*, 2019).

1.2.1 Light Management

Nanomaterials employ two primary strategies to improve light management. The first involves reducing surface reflection using textured antireflective coatings [11]–[14], while the

second involves increasing the optical path in the photoactive layer using resonant or diffractive effects by metamaterials [30–34]. More recently, the use of metasurfaces has gained popularity in TSCs. The active layer can also be used as metasurfaces by introducing gratings in the charge carrier transporting layers to increase the optical performance of the TSC by cumulative effect and guide longer wavelength photons to the bottom cell. Furthermore, can also confine short-wavelength light in the wide-bandgap cell, hence increasing the absorbance.

1.2.2 Metasurfaces

Metasurfaces are 2D- structures composed of resonators or scatterers with subwavelength sizes intended to control the propagation of light. Metamaterials allow for the customization of the dispersed light field, resulting in enhanced light trapping, coupling, and steering within 2T or 4T perovskite/Si. This approach increases light absorption near the top cell's bandgap and enhances near-infrared spectral band transmission to the bottom cell thereby increasing PCE by 6-10% [22], [23] The metasurfaces proposed in the study include three stacked layers. Metamaterial cells at the upper layer alter the electromagnetic wave's refractive index. Incoming light is trapped in a cavity within the intermediate active layer. A near-infrared spectrum is transmitted from the bottom layer to the bottom cell. By adjusting the design of the resonator, the EM properties such as permittivity (ϵ) and relative permeability (μ) of the metasurface can be achieved, resulting in improved parameters such as impedance (z) and refractive index (n). A significant amount of absorption results from the minimization of both the transmission coefficient and the reflectance. The Drude-Lorentz model or the EM properties are extracted from the resonator structure using the S-parameter. [24].

$$z = \pm \sqrt{\frac{(1 + S_{11})^2 - S_{21}^2}{(1 - S_{11})^2 - S_{21}^2}} \quad (1.1)$$

$$e^{ink_0d} = \pm \frac{S_{21}}{1 - S_{11} \frac{z-1}{z-2}} \quad (1.2)$$

$$n = \frac{1}{k_0d} \left[\left\{ \left[\ln e^{ink_0d} \right]'' + 2m\pi \right\} - i \left[\ln (e^{ink_0d})' \right] \right] \quad (1.3)$$

Where '' is the complex conjugate, S_{11} and S_{21} are reflections and transmission's coefficients, k_0 is the range of wavenumber, and d is dimensions of the unit cell.

1.3 Optical Optimization

Several computational techniques have been developed to analyze the optical responses of metasurfaces in solar cells, because to the intricate tandem construction and expensive fabrication. Using simulation tools and algorithms is essential as experimental techniques often use a costly and time-consuming trial-and-error approach, given the many parameters involved. Calculations based on the first principle [25], [26], density function theory [27], and Monte Carlo have been effectively used in the design areas, despite requiring excessive time and computation [28]. To improve the PCE, key factors such as nano-optical design, thickness, and number of active/intermediate layers, materials engineering, and configuration play a crucial role. These parameters can be optimized using exhaustive search, and local, and global optimization techniques as shown in figure 1.3.

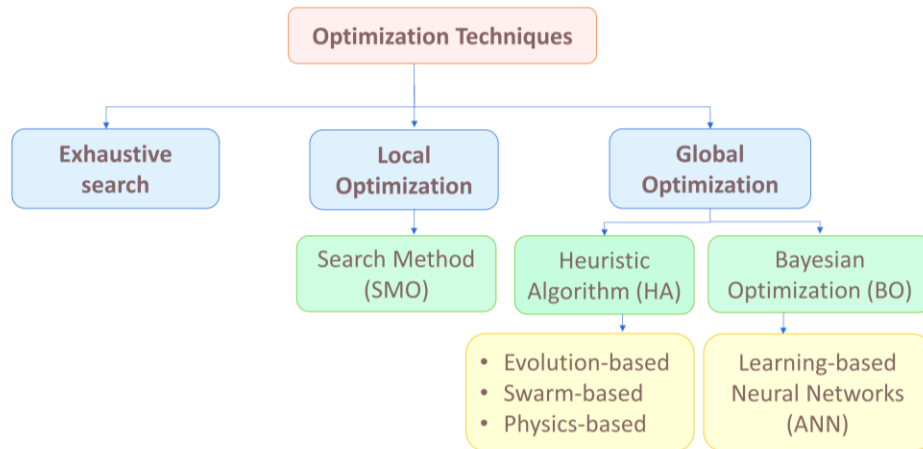


Figure 1.3: Classification of Optical Optimization technique

Optimization methods search the local or global optimum with/without gradient information. Non-linear functions are approximated to near convex values and various parameters can be computed at the same time. An exhaustive search method is used for searching all possible sets of parameters that are sampled uniformly with each step size. Furthermore, larger optimization space can be achieved than exhaustive searches as more samples can be used in the investigation of materials properties and thickness of the active layer to determine thermalization losses [29]–[31]

A learning-based optimization is an offshoot of the Global Optimization technique which uses a data-driven approach to solve complex non-linear optical problems and predict the design space by identifying the best input and unidentified regions with previous information. Artificial Neural Networks (ANN) learn complicated patterns from large amounts of data. There are several layers in which nodes are linked and aggregated which are referred to as the hidden nodes, the input data nodes, and the output neurons. The neuron in the input nodes acquires the datasets that are sent into the system, and the neuron in the hidden layers processes it. Different algorithms and models exploit various complex parameters which are not easily resolved by conventional techniques.

1.4 Problem Statement

TSCs are composed of multiple layers of materials with varying bandgaps to facilitate the absorption of a wider range of solar energy. However, the performance of TSCs is hampered by several factors, including reflective losses, interface losses, and parasitic losses, which ultimately decrease their efficiency and lead to current mismatching. To overcome these limitations, TSCs often require the use of mirrors and lenses to properly concentrate light and achieve optimal efficiency. Recently, the use of nanoscale 2D meta-materials has emerged as a promising alternative to traditional mirrors and lenses. However, the optical optimization of these meta-materials can be both time-consuming, resources, and space-intensive, posing a challenge to their implementation in TSCs.

1.5 Objectives

The research aims to use deep learning for the optical optimization of metasurfaces design and structure optimization of the 2T-Si/Perovskite TSC with less computing power. The main objectives of the research are to:

- Employ deep learning to predict the optical design for the perovskite top cell metasurfaces by forward propagation.
- Search the optimum meta- absorber surface by (opening the ANN black box) inverse design.

- Integrate the findings of the meta-absorber surface with the bottom cell and calculate the current density.
- Compare the efficiency of ANN-generated metasurface design with state-of-the-art literature.

1.6 Significance and Contribution

The integration of Deep Learning in the optimization of TSCs is a relatively new research area that has emerged in the past four years. Despite being in its initial stages, this study offers significant potential in providing accurate and efficient computational solutions that can serve as excellent predictors for optimization. By optimizing the optical parameters theoretically, this approach will facilitate the efficient synthesis of TSCs with high power conversion ability, ultimately reducing the cost of trial and error in solar cell fabrication.

1.7 Thesis Organization

In Chapter 2, the history of metasurfaces is explored along with their application in TSCs and the optimization of metasurfaces through deep learning techniques. By literature review the understanding of state-of-the-art metasurfaces and decision of choosing parameters became clearer. Chapter 3 outlines the research design and methodology employed in the study, including the techniques, tools, and equipment used. The methodology is divided into five steps, which include data collection, processing, forward propagation, inverse design, and explanation, as well as the integration of findings with the solar cell. The first four steps are related to optical optimization of metasurfaces for light management.

In Chapter 4, the mathematical calculations and derivations for simulations are provided, along with details of the simulation setup, material properties, and design of nanophotonic metamaterials operating in the wavelength range of 400nm-1200nm. Ten thousand different structures were simulated using 3-D FDTD simulations in ANSYS Lumerical v202. Several CNN architectures were used to find the best hyperparameters that give low mean square error. Chapter 5 focuses on the 2D-CNN architecture, mathematical calculations, and derivations for the layers of neural network, learnable parameter considered for forward propagation and predictions of nanophotonic structures. Finally, Chapter 6 presents the results and discussions of the FDTD simulations,

including the model architecture, the best-performing hyperparameters, the simulation setup, material properties, and design of nanophotonic metamaterials.

Chapter 2:

Literature Review

This Chapter focuses on the history of metasurfaces, their application in TSC, optimization of metasurfaces by deep learning. and The best combination for highly efficient double-junction TSCs is top cells 1.7–2.3eV bandgap and rear cells 1.12eV [6]. So, c-Si and perovskite are the best choices for the bottom and top cells, respectively, in tandem configuration [7]. The experimental PCE is significantly lower than the theoretically calculated potential. Recent advancements in PV technology have introduced a new type of absorber that optimizes solar energy's ability to be absorbed across the whole spectrum. While traditional solar cells require the use of mirrors and lenses to properly concentrate light and achieve maximum efficiency, this approach is both time-consuming and space intensive [32].

2.1. Review of Metasurfaces

Other highly efficient solar cell structures made from perovskites have been developed, but they suffer from low durability, instability, and narrowband absorption, resulting in decreased efficiency. To address this challenge, researchers have turned to metasurface structures made from metal or dielectric materials, which have shown promising results for broadband absorption [33]. Two-dimensional metasurfaces have proven to be a better option for absorbing incoming electromagnetic waves within a specific frequency band. The efficiency of solar cells can be improved by modifying the metasurfaces' dimensions, form, distance, and substrate medium properties.

Resonant behavior in metasurfaces enables them to achieve special EM properties over constrained frequency ranges. A metallic split ring resonator (MSRR) was used to demonstrate the first-ever ideal absorber operating across a specific frequency range and a thin wire sandwiched between a dielectric substrate was performed by Landy in 2008 [34]. To boost bandwidth in the Gigahertz frequencies range, researchers have examined several configurable split-ring resonator topologies.

Frequency-reconfigurable MSRRs and a pair of directors were designed to have a wide frequency band of operation (microwave region) and can be reconfigured by changing the orientation of the SRRs [35]. Huang proposed the optical design of broadband metasurfaces for permittivity-sensitive solar cell applications. The design comprises three layers of metamaterials with varying refractive indices to increase the absorption in the terahertz frequency range optimized by using a genetic algorithm [36]. Wang characterized and designed an ultra-broadband resonator displaying a near-infrared (NIR) frequency range insensitive to polarization and incident beam angle [37]. Matsumori and Fujimara Over a wide spectrum of visible wavelengths, experimentally observed absorption spectra demonstrate a high absorbance efficiency that is up to 90% from 300 nm to 1500 nm, which is attributed to the localised surface plasmon resonators are excited in the semi-shell MIM structure [38]. Cao simulated absorber composed of a tungsten layer deposited on top of a SiO₂ substrate, with a periodic arrangement of meander-ring resonators. The simulation results demonstrate the excellent performance of the proposed absorber, which can potentially be used in various optoelectronic devices [39].

There has recently been a rise in interest in TSC and metasurfaces working together over the past few years. Metasurfaces have shown the potential in improving light absorption and enhancing the efficiency of solar cells. As per Hossain et al [40], metal-oxide metasurfaces is a revolutionary method for raising perovskite TSC's effectiveness. The authors demonstrate that the use of non-resonant metasurfaces can enhance light absorption and reduce the reflection losses in perovskite solar cells. The metasurfaces are designed using titanium dioxide and silver, which exhibit high refractive index and low reflectance, respectively. The proposed meta-surface design is experimentally demonstrated to increase the PCE of the perovskite TSC by up to 25%. Neder [41] presents the design, fabrication, and characterization of a 4T-perovskite/Si TSCs with an integrated meta-grating spectrum splitters. The meta grating acts as a wavelength-selective filter, allowing greater intensity photons to enter the Si cell and reflecting photons with lower energy that a perovskite cell will absorb. The TSC demonstrated a PCE of 23.6%, which is among the highest recorded efficiencies for perovskite/SiTSCs. Wang et al., [42] present a dual-layer meta surface with a subwavelength periodic array of gold nano disks on top of a thin HOIP film. The simulation findings conclude that the proposed metasurfaces exhibit a significant enhancement of the absorption of HOIPs across a broad spectrum of incoming angles and frequencies.

2.2. Review of Deep Learning in Optical Optimization of TSC

Hubel and Wiesel experimented in 1959 to investigate the processing of visual information in the cat's visual cortex as they moved a bright line in front of it. They discovered that certain neurons known as simple cells responded to a particular angle of the bright line, while others, called complex cells, fired regardless of the light's angle, indicating a detection of movement. It was discovered that complex cells have a hierarchy of functions and acquire inputs from numerous simple cells [43]. Their contribution to understanding the brain's hierarchical structure was awarded a Noble Prize for their work in 1981.

In 1988, A multilayered neural networks called the Neocognitron was created by Fukushima designed for recognizing handwritten Japanese characters, which was motivated by the layered organization of both sophisticated and simple cells [44]. Initial CNN with an algorithm for training was the Neocognitron. Later, the approach known as backpropagation was presented by LeCun et al. [45], allowing for the training of CNNs. After outperforming competing models and algorithms in the Visual Recognition Challenge (ILSVRC), CNNs became incredibly popular [46]. Several CNN architectures that won the contest include AlexNet [47], GoogLeNet and VGG [48] [49], and ResNet [50].

Most of the examples of using learning approaches in TSC design challenges have only recently been put forward making the idea relatively fresh. One of the greatest optimization problems, the thickness of active layers and interfaces has been addressed previously by iterative searches [29]–[31], [51]. On the other hand, learning-based methods save optimization time compared to local search optimization. Several studies [52]–[54] have undertaken optimization of the thickness of interface layers and active layers of TSC. Chaudhary et al., [52] compared the PCE measures of the Si TSC cell's output parameters generated by SCAPS and ANN (trained by BO). H. Q. Tan *et al.* [54] also reduced computational cost by concentrating on the crucial parameters and forecasting the ideal design for a bifacial 4T-perovskite TSC by using ANN trained by Bayesian optimization. C. Yi *et al.* [53] also reported an quick, incredibly precise, and computational resource-saving approach to examine the efficiency of TSC. The experimental J_{sc} and PCE of TSC with the optimum active layer thickness can achieve up to 15.79 mA/cm² and 23% respectively, and PCE can be improved to 28%. Table 2-1 shows the comparison of recent state-of-the-art papers that use ANN to optimize the thickness, configuration, composition, and

design of TSC.

Table 2-1: Learning-based Methods for TSC Optimization

Ref.	Method	Simulation	Input	Output	MSE
[52]	ANN contains 1 hidden layer and 40 neurons.	MATLAB and SCAPS for validation with 3600 Training dataset, 1028 Validation Set	<ul style="list-style-type: none"> ▪ Jsc ▪ Temperature ▪ Thickness 	Current Density	0.0037
[53]	ANN (15-layered) with 5 hidden layers.	FDTD for numerical simulations with 12,500 Training datasets.	Thickness of <ul style="list-style-type: none"> ▪ Glass, ITO ▪ PCBM ▪ Perovskite 	Current Properties	0.052
[54]	ANN 2 hidden layers	TMM and raytracing simulations	Thickness of <ul style="list-style-type: none"> ▪ Perovskite ▪ ARC 	PCE	-
[55]	CNN (100 hidden fully connected neurons) 4 convolutions	Vienna Ab initio Package for structural parameters containing 862 Training dataset	<ul style="list-style-type: none"> ▪ 380 different Perovskite ▪ Crystal Structure ▪ Lattice constant 	Band gap, lattice constants and crystal angles	0.02
[56]	Bayesian optimization	Local Optimization for thickness	<ul style="list-style-type: none"> ▪ Aspect ratio ▪ ARC 	Textured interfaces.	-

2.3. Critical Analysis

The authors of the study [55]–[57] identified certain limitations in the optical optimization of TSCs considered when selecting parameters for current research. They found that by optimizing the metasurface, parasitic and reflective losses in 2T-perovskite/Si TSCs were reduced by an impressive 62%. However, it is important to note that the computational cost increases as the size and variability of the input vector $f(x)$ increase. The optimization process requires exploring an extensive parameter space, including variables such as n , FF, (p/n) , band gap, and more, which further adds to the computational burden. Moreover, incorporating multiple design parameters in a 3D-framework intensifies the computational load. Additionally, the computation of effective diffusion length is impacted by photo-induced carriers at the surfaces, leading to lower sub-cell performance. It is worth mentioning that the study did not consider the effects of defects, and instead, an ideal solar cell architecture was used as a reference point for comparison.

Chapter 3:

Methodology

This chapter focuses on the research design, methodology, techniques, tools, and equipment used in the research work. The methodology is divided into 5 steps: Data collection, processing, forward propagation, inverse design, explanation, and integration of findings with the solar cell.

3.1. Research Design

The methodology is comprised of 5 steps as shown in Figure 3-1. The first step is data collection which involves simulating the metasurfaces. The design parameters such as the resonator's width, length, and arm tips are chosen to achieve resonance and maximum absorption in the bandgap region. The parameter's range is set comparable to the light's wavelength. The second step is data processing. The third step is the most crucial as hyperparameters are essential components for ensuring accuracy and low MSE. Nine model architectures were tested, and the best-performing model was used for predictions and SHAP (Shapley Additive Explanations) explanations. In the fourth step, the SHAP-validated design was integrated with the bottom low-bandgap cell to find metrics such as J_{sc} , fill factor, etc. Lastly, the performance of the standard TSC with and without the metasurfaces was compared.

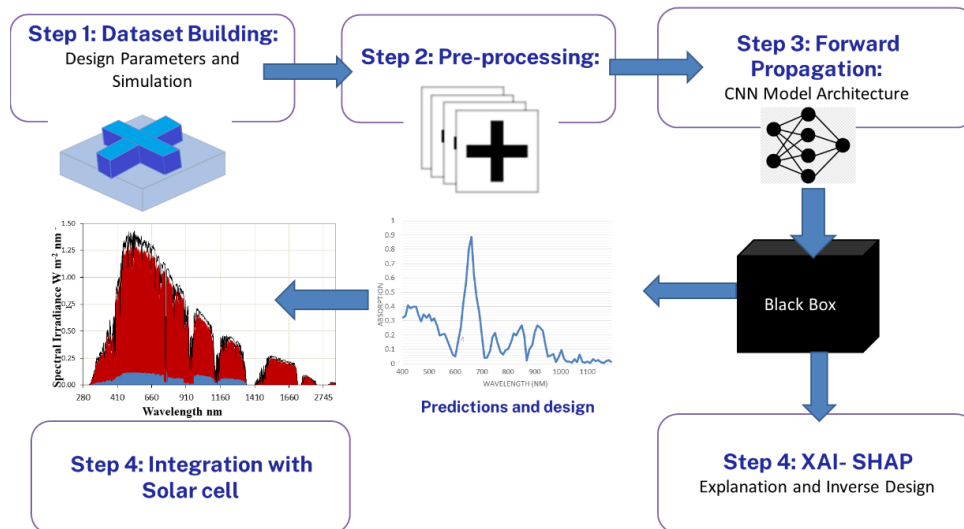


Figure 3.1: Methodology Steps and Research Design

3.2. Building Dataset

The dataset is composed of 10,578 different metasurfaces geometries. The parameters considered are the height, width, and arm lengths of the resonator. The parameters are defined in detail in Chapter 4. The 3D-FDTD simulations were performed to achieve 80-point absorption spectra of metasurfaces in ANSYS Lumerical v202. The geometry of the resonator was cross, square, L-shaped, window-shaped polygon and their inverted version consisting of 14, 4, and 29 vertices respectively. The simulation mesh size and unit cells dimensions are given in table 3-1. The shapes were chosen because of the ease of fabrication by the lithography technique. Each meta structure contains a 100nm Titanium dioxide (TiO_2) hole transporting layer (h_1), 250nm wide band gap Perovskite ($\text{CH}_3\text{NH}_3\text{PBr}_3$) middle layer (h_2), and 100nm top resonator Zinc oxide (ZnO) (h_3) different designs parameter as shown in figure 3.2.

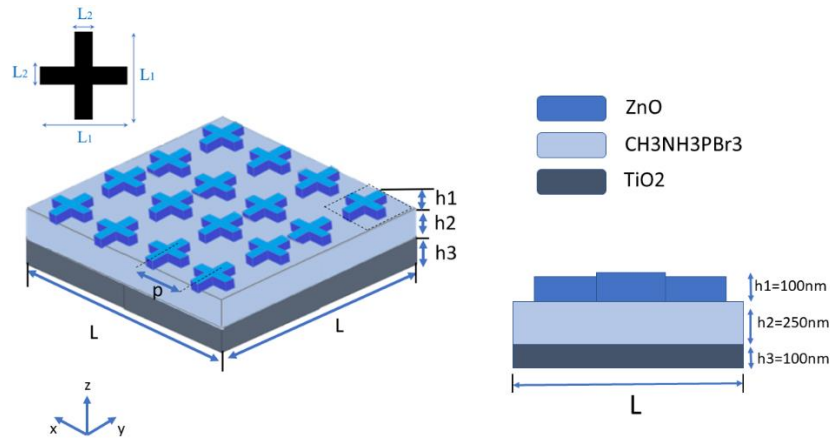


Figure 3.2: Metasurface Design (Left) with the 3D view and xz view (Right)

Table 3-1: Simulation Source, Unit cell dimension and Mesh setting

Info	Denotation	Number
Number 3D-FDTD Simulations	n	10,578
Unit Cell Dimensions	L	100-3200nm ²
Simulation Mesh Step Size	dx, dy	50nmx50nm
Resonator Mesh number region	dl _x , dl _y , dl _z	75nmx75nmx202nm
Source Wavelength	λ	400-1200nm

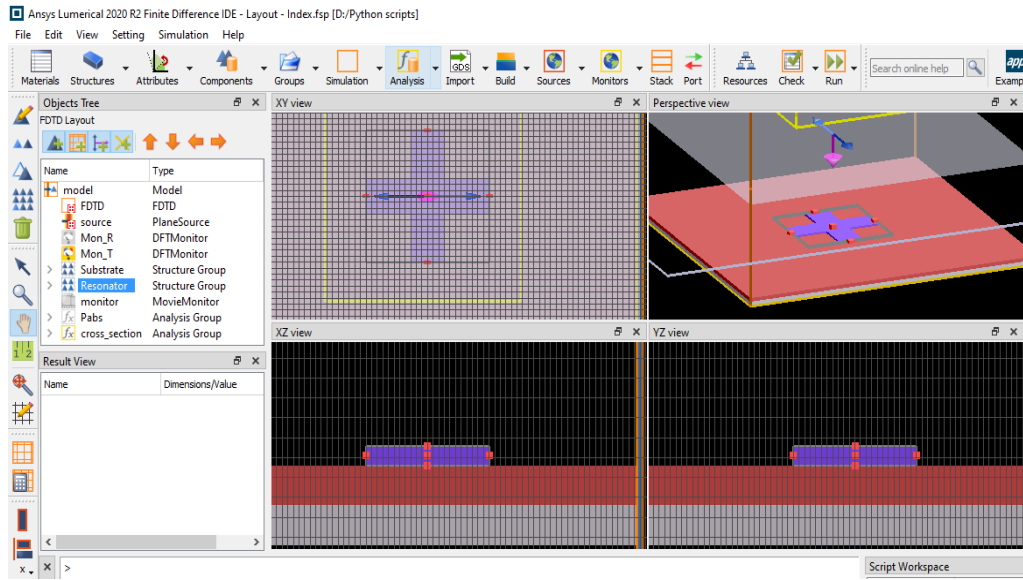


Figure 3.3: Interface of ANSYS FDTD software (Left) with the 2D view xy and and xz view of metasurface 3D perspective view (Right)

3.3. Dataset Pre-processing and Splitting

Data pre-processing is an essential step in deep learning, which ensures the quality of the input data, which ultimately impacts the accuracy of the model. Pre-processing involves various techniques such as data normalization, feature scaling, data augmentation, and dimensionality reduction. Normalization involves scaling the data to have zero mean and unit variance, while feature scaling scales features to the same range. Data augmentation techniques like flipping, rotating, or cropping the images can help increase the size of the dataset and prevent overfitting. The images were converted to a greyscale 40 x 40 x 1-pixel image. Each pixel contains the minimum feature size of 80nm which lies within the fabrication range. The dataset was split (9:1) ratio. 90% of the dataset was used for training CNN while 10% was used for validation.

3.4. CNN Architecture and Forward Propagation

The 2D-CNN architecture was chosen because of the 2D-input dimensions. A 2D-CNN has four basic layers: The input layer, the discrete Convolution layer, the pooling layer, and the fully connected layer. Different CNN architectures generate different feature map responses in corresponding layers. Nine models were used with different architectures to find out the best hyperparameters that gives low MSE. Each CNN architecture was coded in Python 3.6 and was

implemented in TensorFlow 1.14 and Keras library. The code was adopted from the study of Christopher Yeung’s study [58] and Raman Lab Github which was modified and executed for forward propagation. The hyperparameter search was done in Google Collab and the best architecture was run in the deep learning laboratory, SEECS. The specs of the PC are given below in figure 3.4:

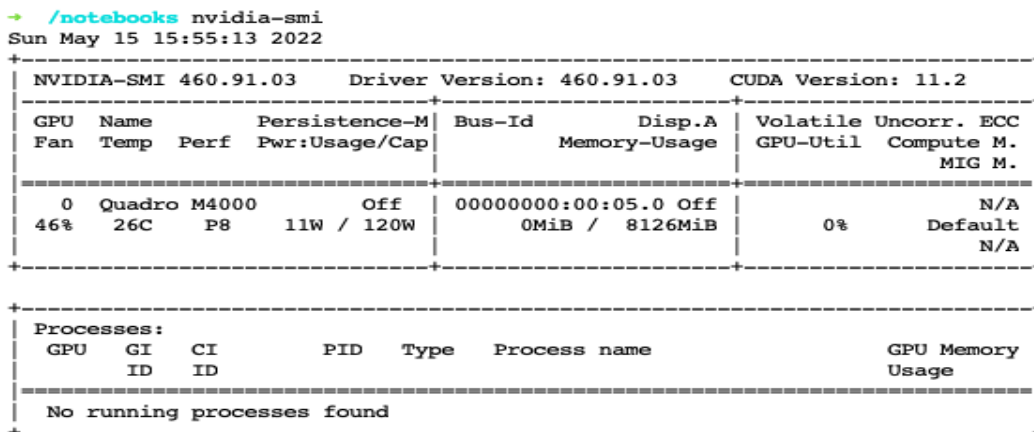


Figure 3.4: Specs of Google Collab (Left) and PC used for training Dataset (Right)

3.5. Inverse Design (Opening CNN Black Box)

For opening the black box of the best-performing model, the SHAP framework was used. It is derived from game theory which gives unified explanations. Detailed analytical expressions used for generating heat maps are discussed in Chapter 5. Deep SHAP incorporates DeepLIFT, a technique that was previously used to split predictions into outputs using Shap parameters and backpropagation. The validated top contributing SHAP values in the region 400-800nm were extracted and converted into binary maps which were imported in Lumerical for getting absorption spectra as shown in figure 3.5.

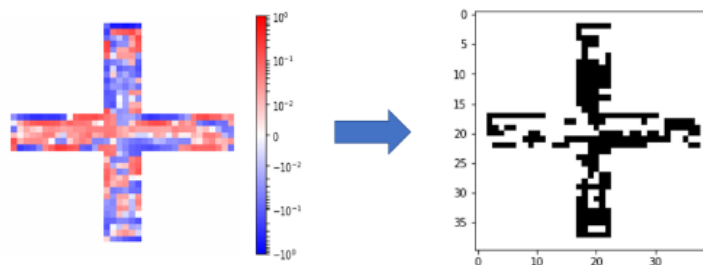


Figure 3.5: Reconstructed image validated top contributing SHAP values

3.6. Integration of Metasurface with Solar cell

The designed metasurfaces were integrated into the typical reference TSC architecture. The optical model employed is examined by showcasing all the physical parameter values that can be extracted using the simulation model. Lastly, the performance of the standard TSC with and without the metasurfaces was compared. The solar simulations were carried out using SCAPS-1D with separate def file run by single tandem connection script as shown in figure 3.6.

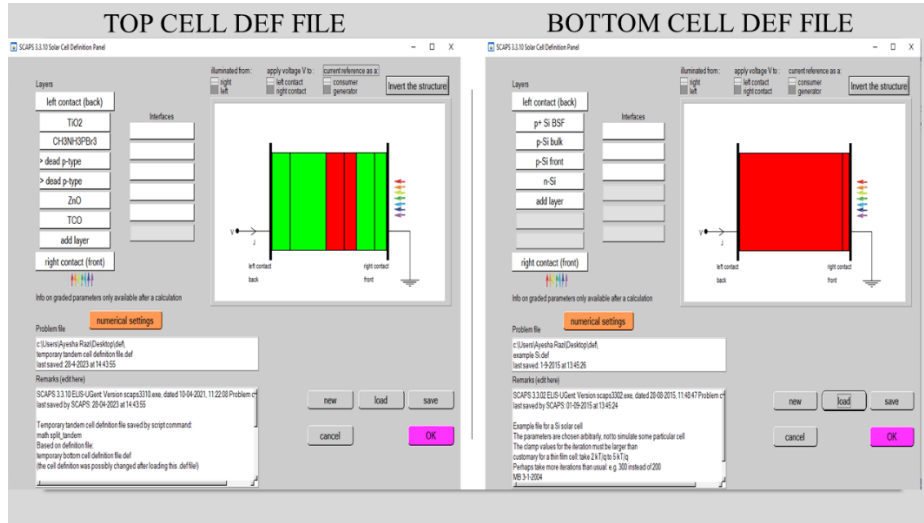


Figure 3.6: Top and Bottom cell def file of TSC in SCAPS-1D

3.7. Software, Equipment, and Tools Details

Details about the Equipment/ Software used are given below in table 3-2.

Table 3-2: Details about Equipment/ Software

Methods	Software/Equipment	Source
3D-FDTD Simulations	ANSYS Lumerical v202	University of Arizona
2D image generation of resonator	MATLAB	-
Image Pre-processing, CSV	OpenCV, OS, Pandas	-
Model Architecture Execution	Tensorflow 2.2.1, 1.14, Keras Library 2.3.0	Jupyter Notebook
GPU Information	NVIDIA K80/T4	SEECs, Collab
XAI SHAP explanation	SHAP 0.31.0	-
Solar cell simulation	SCAPS-1D v3310	Marc Burgelman

Chapter 4:

Analytical Expressions and Numerical Methodology for Simulations

This chapter focuses on the mathematical calculations and derivations for simulations, details of simulation set-up, material properties, and design of nanophotonic metamaterials operating in wavelength range 400nm-1200nm. 3-D Finite difference time domain (FDTD) simulations of ten thousand different structures were performed in ANSYS Lumerical v202.

4.1. Mathematical Expressions for Simulations

The calculation for the absorption per unit volume of the metasurfaces the surface integral of the Poynting vector is taken. The dimensions for the absorption per unit volume at a given wavelength are (x, y, z, w).

4.1.1. Time-averaged Instantaneous Poynting Vector

The Poynting vector is an energy flux vector for electromagnetic (EM) energy in space as a function of time. According to Poynting's Theorem, the pointing vector is represented as:

$$\frac{\partial u}{\partial t} = -\nabla \cdot S - J_f \cdot E \quad (4.1)$$

where S is the pointing vector, u is the energy density of the EM field, J_f is the free charge current density and E is the electric field. Eq (4.1) can also be written as the following equation for electromagnetic energy density for dispersive materials with permittivity (ϵ) and permeability (μ).

$$u = \frac{1}{2}(\epsilon E + \mu H) \quad (4.2)$$

Sinusoidal electromagnetic wave propagation with varying amplitude and angular frequency (ω) can be notated in the form of phasor S_m .

$$S_m = \frac{1}{2} E_m \cdot H_m^* \quad (4.3)$$

where, E_m is phasor for instantaneous sinusoidal electric field propagation, $*$ is a complex conjugate, and the real instantaneous sinusoidal electric field is denoted as $E_m e^{j\omega t}$ while the real magnetic field $H_m e^{j\omega t}$. The instantaneous pointing vector is derived as follows:

$$\begin{aligned}
 S_t &= E_t \cdot H_t \\
 S_t &= \text{Re}(E_m e^{j\omega t}) \cdot \text{Re}(H_m e^{j\omega t}) \\
 S_t &= \frac{1}{2} (E_m e^{j\omega t} + E_m^* e^{-j\omega t}) \cdot \frac{1}{2} (H_m e^{j\omega t} + H_m^* e^{-j\omega t}) \\
 S_t &= \frac{1}{2} \text{Re}(E_m \cdot H_m^*) + \frac{1}{2} \text{Re}(E_m \cdot H_m e^{2j\omega t})
 \end{aligned} \tag{4.4}$$

For time-averaged instantaneous pointing vector Eq (4.4) is written as follows:

$$\langle S \rangle = \frac{1}{T} \int_0^T S_t dt \tag{4.5}$$

$$\langle S \rangle = \int_0^T \left[\frac{1}{2} \text{Re}(E_m \cdot H_m^*) + \frac{1}{2} \text{Re}(E_m \cdot H_m e^{2j\omega t}) \right] dt \tag{4.6}$$

Eq (4.6) can be written as follows when double frequency $(E_m \cdot H_m e^{2j\omega t}) = 0$

$$\langle S \rangle = \frac{1}{2} \text{Re}(E_m \cdot H_m^*) \tag{4.7}$$

By substituting eq (4.6) with eq (4.3), the time-averaged instantaneous pointing vector can also be written as:

$$\langle S \rangle = \text{Re}(S_m) \tag{4.8}$$

4.1.2. Divergence of Poynting Vector and Absorption per unit Volume Calculations

For the calculation of absorption per unit volume, the surface integral of the Poynting vector is taken. The absorption per unit volume at a given wavelength and dimensions (x, y, z, w) is written as:

$$\frac{A}{V} = \langle S \rangle$$

The equation can also be expressed as:

$$\frac{A}{V} = -\frac{1}{2} \text{Re}(E_m \cdot H_m^*) \tag{4.9}$$

The negative sign in the equation is due to the surface integral of the Poynting vector, as the area is pointing outwards while the EM wave is going in the opposite direction. In FDTD simulations, absorption is calculated as a function of frequencies and space. The electric intensity and index of the material are needed to carry out simulations [59]. The calculation by divergence vector gets complicated numerically and requires much memory. So, a more numerically intensive equation is used to carry out the simulation:

$$\frac{A}{V} = -\frac{1}{2} \text{Re}(iE_m \omega \cdot H_m^*) Y \quad (4.10)$$

4.2. Material Properties

Table 4-1. shows the material properties used for simulations. different design parameters are given in section 4.2. The reason for selecting TiO₂ and ZnO is that the materials have good thermal stability, high hole transportation capacity, and energy level matches incredibly with Perovskite as can be seen from the energy band diagram Figure 4.1. The material properties and real refractive indices of perovskite were taken from experimental data [60].

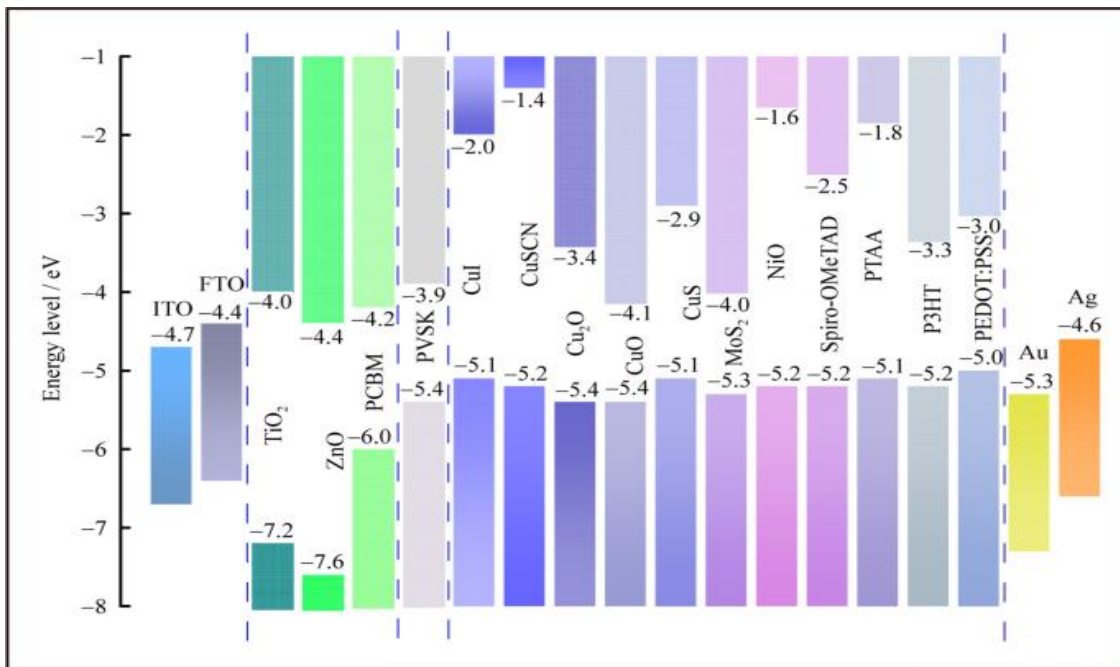
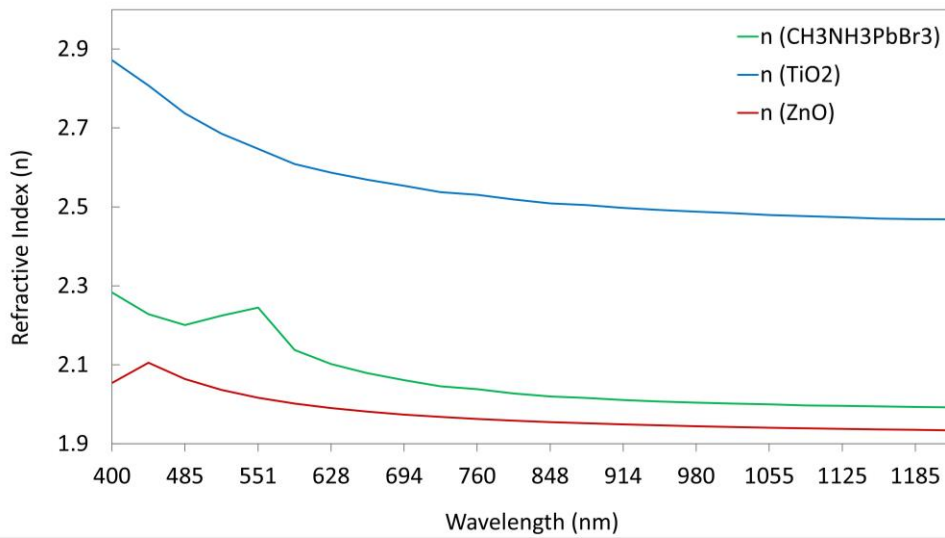


Figure 4.1: Energy band diagram of Materials used in Perovskite Solar Cells [61]

Table 4-1: Material Properties used for Simulations

Materials	Thickness (nm)	Permittivity (ϵ)	Extinction coefficient (k)	Reference
$\text{CH}_3\text{NH}_3\text{PbBr}_3$	250	4.6112	0.213	[60]
ZnO	100	5.23	0.04	[62]
TiO_2	100	-	0.013	[62]

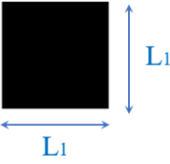
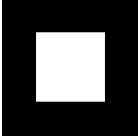
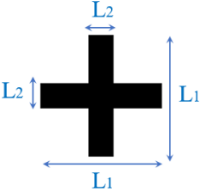

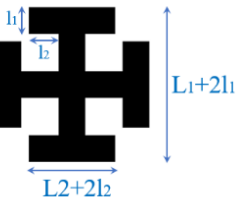


**Figure 4.2:** Refractive index of perovskite, zinc monoxide and titanium dioxide at wavelength (400nm-1200nm)

4.3. Metasurface Simulation Set Up

The 3D-FDTD simulations were performed to achieve 80-point absorption spectra of 10,578 different metasurfaces in ANSYS Lumerical v202. The geometry of the resonator was cross, square, L-shaped, window-shaped polygon and their inverted version. The shapes were chosen because of the ease of fabrication by the lithography technique. The 2D- array images of these metasurfaces were generated in MATLAB. The mesh step size of 100nm was maintained in all three dimensions. Periodic boundary conditions were applied in x and y dimensions while PML condition was applied on the z-axis to absorb/ transmit maximum light with minimum reflection. Each shape was converted into a greyscale 40 x 40 x 1-pixel image. Each pixel contains the

minimum feature size of 80nm which lies within the fabrication range. The plane wave source was injected along the z-axis with wavelength 400nm-1200 nm. The detailed parameters of the design were in the range of 100nm²-3200nm² periodic arrays as shown in table 4-2.

Table 4-2: 2D images of metasurface unit cell shapes and their design parameters

Designs	Inverted Versions	Parameters	Simulations
		Length of shape (L_1) = 100nm-3200nm/100nm	n=898
		Length of shape (L_1) = 100nm-3200nm/100nm Length of arms (L_2) = 100nm- L_1 /100nm	n =4390
		$L_1 = 100\text{nm}-3200\text{nm}/100\text{nm}$ $L_2 = 100\text{nm}-L_1/100\text{nm}$ Length of perpendicular arms (L_3 & L_4) $L_3=L_1+2l_1$ $L_4=L_2+2l_2$	n =4456
	-	Length of shape (L_1) = 100nm-3200nm/100nm Length of shape (L_1) = 100nm-3200nm/100nm	n =834

4.4. Solar Cell Simulation Set Up

The designed metasurfaces were integrated into the typical reference TSC architecture consisting of the following structure. The top cell consists of Transparent Conducting Oxide TCO (200nm), ZnO resonator (100nm), CH₃NH₃PBr₃ (250 nm), and TiO₂ (100 nm). The bottom cell

consists of n-Si (150nm), p-c- Si bulk (350nm), p+ Si rear Back surface field BSF (50nm), and gold contacts. Figure 4.3. shows the schematic representation of the 2T-TSC. The optical model utilized is evaluated by presenting all the physical parameters obtained through the simulation model. Table 4-3 shows the properties of materials used in TSC simulation. The calculations were performed in a Solar cell capacitance simulator (SCAPS-1D) and Lumerical. The experimental setup involved the use of a Solar spectrum AM 1.5G source, which provided a consistent electromagnetic field across the solar cell stack from 400 to 1200 nm wavelength range. For different simulated solar cell structures, the mesh size was adjusted based on their respective architectures, with larger mesh sizes employed for some structures. Override mesh regions were placed at critical interfaces and resonators to ensure high simulation accuracy.

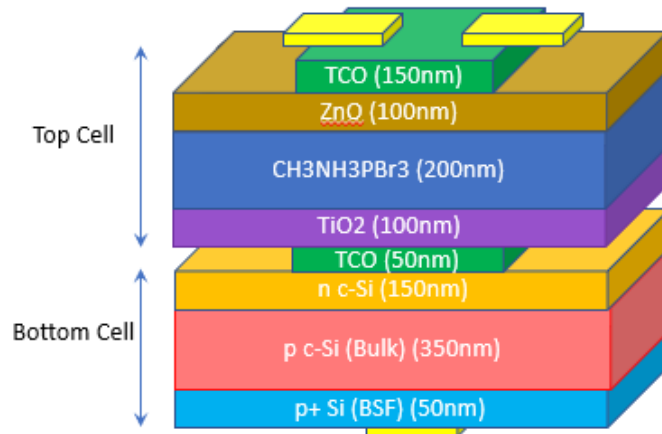


Figure 4.3: Schematic representation of the 2T-Si/perovskite TSC

Table 4-3: Properties of materials used in TSC simulations

Material	Band gap (E _g) (eV)	Electron Affinity (eV)	Dielectric Permittivity (ε _r)	Electron Thermal velocity (m/s)	Auger Capture Rate (cm ⁻⁶)	Reference
TCO	3.2	4.3	9.7	1.2 x 10 ⁷	2.7 x 10 ⁻³¹	[63]
ZnO	3.4	4.3	8.6	1.5 x 10 ⁷	2.0 x 10 ⁻³¹	[64]
CH ₃ NH ₃ PbBr ₃	2.3	3.9	25	1.0 x 10 ⁷	1.0 x 10 ⁻³⁰	[65]
TiO ₂	3.1	1.59	86	1.0 x 10 ⁷	2.0 x 10 ⁻³¹	[65]
p-Si	1.2	4.04	4	1.0 x 10 ⁷	1.0 x 10 ⁻³⁰	[66]

Assuming that all the dopant impurities in Si are ionized, for n-type $n_o \approx N_D$ which can be written as minority charge carriers $p_o = n_i^2/n_p$. At thermal equilibrium, fermi energy is expressed as: $E_f = E_i + k_B T \ln \left[\frac{N_D}{n_i} \right]$ where N_D is the donor impurity for n-type. : $E_f = E_i + k_B T \ln \left[\frac{N_A}{n_i} \right]$ where N_A is the acceptor impurity for p-type. The built-in potential can be expressed as the difference between the Fermi energies in the doped regions, resulting in a potential difference across the junction, denoted as V_{bi} .

$$eV_{bi} = E_f^n - E_f^p = E_g - k_b T \ln \left[\frac{N_c}{n_o} \right] - k_B T \ln \left[\frac{N_v}{p_o} \right] \quad (4.11)$$

Eq (4.11) ca also be written as:

$$eV_{bi} \approx k_b T \ln \left[\frac{N_A N_D}{n_i^2} \right] \quad (4.12)$$

The total optical power absorbed (Q) is measured by the expression:

$$Q = \int Abs(\lambda) F(\lambda) d(\lambda) \quad (4.13)$$

Where Abs is wavelength-dependent optical absorption. Absorption is dependent upon reflection $|S_{11}|^2$ and transmission $|S_{21}|^2$. $Abs(\lambda) = I - R(\lambda) - T(\lambda)$. By utilizing $Abs(\lambda)$, a spectrum that indicates the absorption in each layer of the solar cell stack is derived. Based on this absorbed light, key quantities such as the charge carrier generation rate (G) and short-circuit current density (J_{sc}) can be determined through appropriate calculations.

$$G = \int_{\lambda_{min}}^{\lambda_{max}} \frac{\lambda}{hc} Abs(\lambda) I_{AM1.5}(\lambda) d\lambda \quad (4.14)$$

$$J_{sc} = QG \quad (4.15)$$

where, The Planck's constant (h), speed of light (c), AM1.5 (λ) solar spectrum, and elementary charge (Q) is used to calculate the charge carrier generation rate (G) and short-circuit current density (J_{sc}) from the absorbed light spectrum obtained using $Abs(\lambda)$. The J_{sc} value is a measure of the solar cell's optical performance and represents the maximum current density that the Si/perovskite tandem solar cell can achieve based on its optical properties alone. The charge carrier generation rate (G) can be represented in the form of a one-dimensional (1D) or two-dimensional (2D) profile that is a function of position and/or incoming light wavelength values.

Chapter 5:

Arithmetic of CNN

This chapter focuses on the 2D-CNN architecture, mathematical calculations, and derivations for the layers of neural network, learnable parameter considered for forward propagation and predictions of nanophotonic structures.

5.1. 2D-CNN Architecture

CNNs are heavily dependent on affine transformations. This procedure involves taking a vector as an input and multiplying it by a matrix to get an output. Typically, a bias vector is added before the result is passed through a function of nonlinear activation. This can be used for any form of input like images, videos, audio files, or a set of disorganized features - these can all be flattened into a vector before the transformation occurs. A 2D-CNN has four basic layers:

- Input layer
- Discrete Convolutional layer
- Pooling layers
- Fully connected layer

5.1.1. Input Layer

In a 2D-CNN, the input layer receives the input layer is multi-dimensional data array represented as width and height. The input is provided to the network in a 2D shape as a matrix rather than being reduced to a 1D vector, making it simpler to capture spatial correlations. The input data have the following features:

- Input is converted into a multi-dimensional data array.
- The dimensions of the array depend on the input data and in the case of images it's represented as width and height.
- A channel axis represents the color of input data. In the case of RGB images, the number of channels is 3 whereas in greyscale images there is 1 channel.

During the transformation, the axes of the input data array are handled equally, and the topological information is not considered. So, 2D images are used which represent the optical geometric design parameters. Color-encoded (RGB) 3D images can also be used which can represent the range of material and structural parameters, and geometric design. The dataset consists of 2D- images of 10,578 TiO₂/MAPBI₃/ZnO metasurfaces. Each shape was converted into a grey scale 40 x 40 x1 pixel image. The shape of the input layer is (10,578, 40, 40, 1). The inputs are denoted as $x_1, x_2, x_3, \dots, x_n$ where, x_n is the total number of inputs and weights applied to the inputs are $w_1, w_2, w_3, \dots, w_n$. The added intercept in an equation with linearity is analogous to bias. Along with the weighted aggregate of the input to the neuron, it is an extra variable in the neural network's algorithm that is used to change the output. The summation equation (5.1) of weight, biases, and input can be written as:

$$a_l = \sum_{l=1}^n w_{ln}^1 x_n + b_l^1 \quad (5.1)$$

where, a is the summation function, l , and superscript 1 represent the first layer of the neural net while b represents the bias annotated to the neuron. The activation function transforms the summation function by using differential and non-linear functions and the hidden layers (z) are a function of these transformations. The most used activation functions are sigmoid, tanh, ReLu, and Leaky ReLu functions. The ReLu function is expressed as $\text{ReLu}(x) = (y) = \max(0, x)$. The values are combined to give a unit activation equation which can be written as equation (5.2)

$$a_k = \sum_{l=2}^M w_{lk}^2 z_l + w_{ko}^2 \quad (5.2)$$

The overall equation of the weighted sum of the neuron containing inputs, weights, and biases is written as:

$$y_k(x, w) = \sigma \sum_{l=2}^M w_{lk}^2 z_l \left(\sum_{l=1}^n w_{ln}^1 x_n + b_l^1 \right) + w_{ko}^2 \quad (5.3)$$

5.1.2. Discrete Convolution

A common technique for analyzing an image is to apply convolution using a filter, which is sometimes referred to as a kernel, to extract the significant features, such as the edges, from the original image. A discrete convolutional layer is a linear transform that uses several kernels in

which a small number of input elements have a significant impact on a particular output elements and identical weights are applied to the input more than once. Figure 5.1. shows input feature map and output feature map. Despite the fact that many feature maps are frequently layered on top of one another, input feature map only depicts an input feature map.

5.1.3. Kernel

As it moves over the input feature map, an input kernel maintains a value slide. To obtain the result at the present site, the outcome of each kernel component and the overlapping input element is calculated at each point. The results are then combined. To produce many output feature map images, this process can be repeated with various kernels. Output map attributes are the end outcome of this technique as shown in figure 5.1. For 2D-input data the kernel is three dimensional, each output feature map is convolved with a separate kernel and the resultant is summed individually to produce an output feature map as shown in figure 5.1. The permutation of the shape of the kernel is expressed as (n, m, k_1, \dots, k_N) , where:

- n= number of the output feature map
- m= number of the input feature map
- k= kernel size (k_1, \dots, k_N) .

The output size of a convolutional layer along the axis, width dimension (j), is influenced by:

- i_j , which represents the size of input along j-axis
- k_j , which refers to the size of kernel size along j-axis
- s_j , which is the stride or the range between the two successive kernel points along j-axis
- p_j , which denotes the zero padding along the j-axis or the number of zeros added at the beginning and end of an axis.

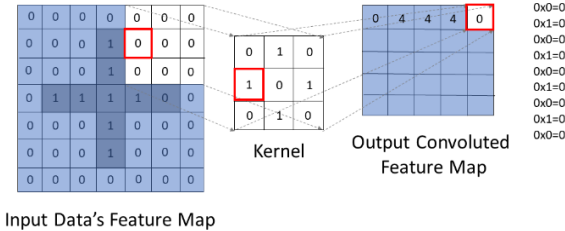


Figure 5.1: Example of a discrete convolution containing a single input and output feature map $(n = m = 1)$ for 2D-convolution $N = 2, i_1 = i_2 = 7, k_1 = k_2 = 3$

Figure 5.2 shows some layouts of the 2D-kernels used in the CNN models. The darker regions represent weight values close to zero while lighter regions represent higher weight values close to one. These values are applied to input data.

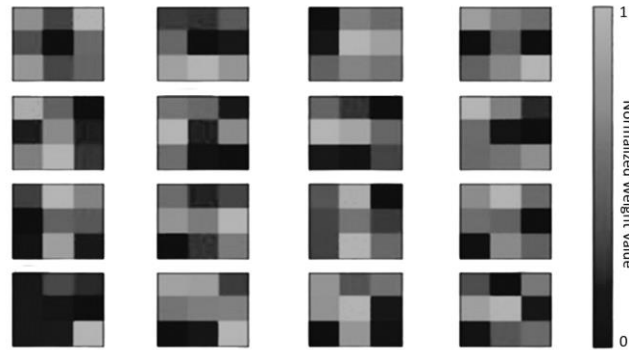


Figure 5.2: Layouts of the 2D-kernels used in the CNN models

Furthermore, in addition to the feature maps, there is a Receptive Field, which is the particular neuron's local three-dimensional patch in the receiving volume. The set of neurons known as the Depth Column all focus on the same region of the source data. Every neuron in a layer of convolution has a unique connection to its localised receptive field, and every neuron in each result feature map uses the same weights as shown in figure 5.3. The motivation for utilizing multiple output feature maps is that each weight can extract distinct features from the input image, such as horizontal or vertical edges.

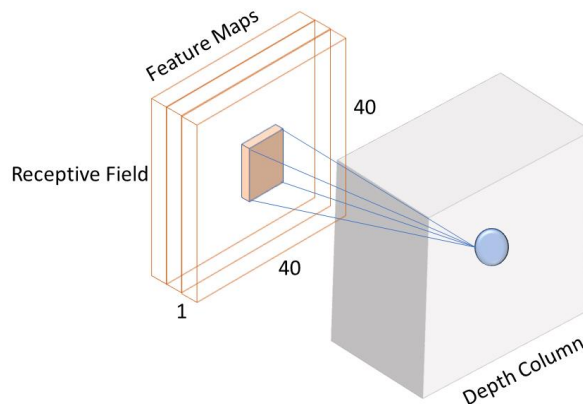


Figure 5.3: Receptive fields in feature map and Depth column

5.1.4. Strides and Padding

Strides are an aspect of subsampling. Strides can alternatively be thought of as a measure of the proportion of the output that is kept, as opposed to how much of the kernel gets translated. For instance, shifting the kernel by two hops is identical to shifting it by one hop while keeping just the odd output parts as shown in figure 5.4. Padding is the number of zeros or numbers added at the beginning and end of an axis to derive output size as kernel slides across the input feature map. No-zero padding was used in CNN models to determine the size of the convoluted output. In this case, the output size is not equal to the input size.

$$o = (i - k) + 2p + 1 \quad (5.4)$$

The zero-padding can be further classified into two major types: same padding and full padding.

a) Same (Half) Padding:

In the same padding, the size of output remains the same as the input's size (i.e., $o = i$) as shown in figure 5.5. For any input size 'i' and for odd kernel size $k = 2n + 1, n \in \mathbb{N}$, unit stride 's = 1' and half padding ' $p = \frac{bk}{2c} = n$ '. The expression is derived by placing the values in equation (5.4) as:

$$o = i + \frac{2bk}{2c} - (k - 1) \quad (5.5)$$

$$o = i + 2n - 2n = i \quad (5.6)$$

b) Full padding:

In full padding, the output size decreases concerning the input size or vice versa as shown in figure 5.6. For any input size 'i' and 'k', and for output size less than input size ' $p = k - 1$ ' and unit stride $s = 1$. The expression is derived by placing the values in equation (5.4) as:

$$o = i + 2(k - 1) - (k - 1) \quad (5.7)$$

$$o = i + (k - 1) \quad (5.8)$$

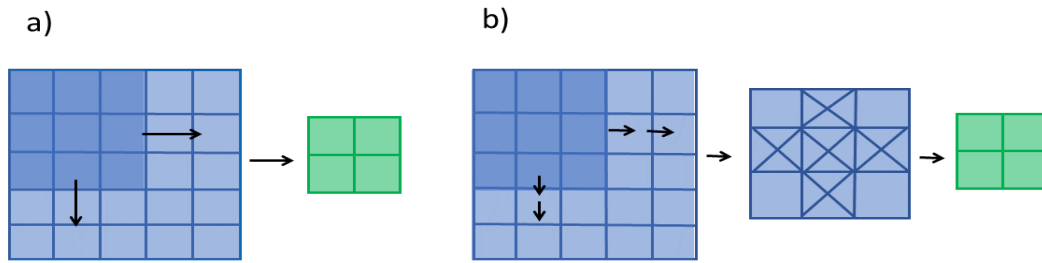


Figure 5.4: a) showing generalized strides where kernel takes 2 steps to give output size 3x3 b) an alternative way of sampling where kernel slides 1 and translated to 2x2 output

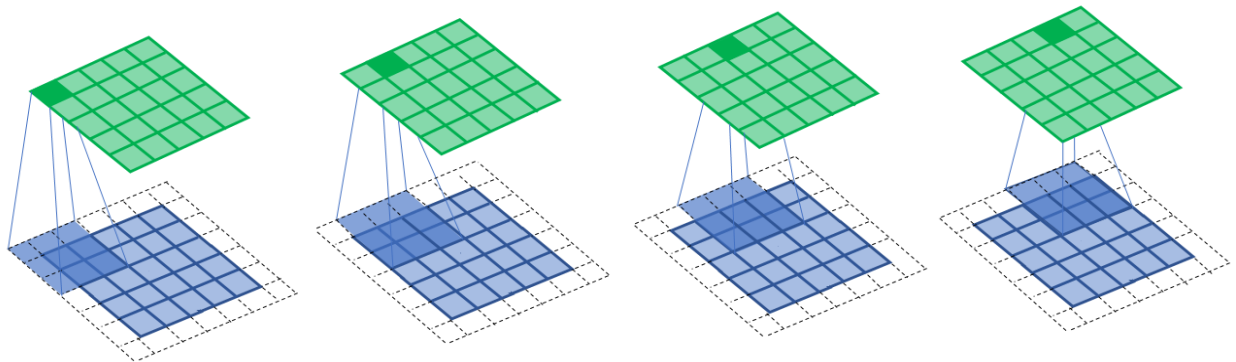


Figure 5.5: showing half padding convolution of a 3x3 filter over a 5 x 5 input (i.e., $i = 5$, $k = 3$, $s = 1$ and $p = 1$)

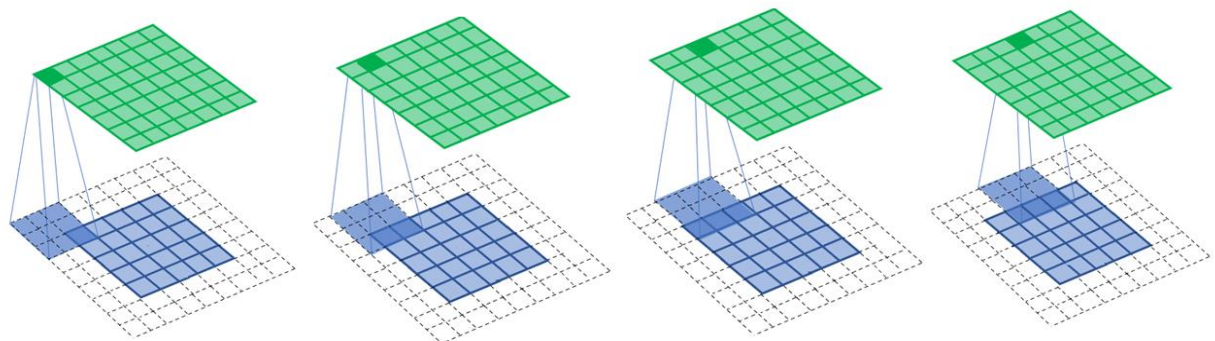


Figure 5.6: showing full padding convolution of a 3x3 filter over a 7 x 7 input (i.e., $i = 5$, $k = 3$, $s = 1$ and $p = 2$)

5.1.5. Pooling Layer

Another crucial component of CNNs is the pooling process. By utilizing a function to split the subregions, by taking the maximum or average product, that reduces the size of feature map which is called avgpool and max pool respectively. Pooling is accomplished by dragging a window across the input to a pooling function. Since pooling involves non-zero padding following expression is used:

$$o = \frac{(i - k)}{s} + 1 \quad (5.9)$$

5.1.6. Fully Connected Layer

The final essential component in a CNN is the Fully Connected Layer, which is composed of completely linked neurons to every activation in the layer before. CNN has many thousands of learnable parameters and internal weights which are calculated for each type of layer. These parameters are represented by a hierarchy of available filters which are utilized to gather information from images. To calculate their activation, there is a matrix multiplication, then a bias offset. The RELU or Leaky RELU Function is the activation function that works best in the preceding layer.

In Figure 5.7, the model's early layers effectively capture boundaries and edge connections. The feature maps, however, become harder to comprehend as the number of layers increases. Understanding the connection between the characteristics extracted and the network's final output gets more and more challenging as the network's layers get deeper. It is challenging to incorporate this information into a thorough justification of the algorithm's decision-making procedure. Analyzing individual filters inside a network to understand the model provides limited value for model interpretation and verification. It's because this method doesn't offer a logical justification for the whole framework or a particular prediction.

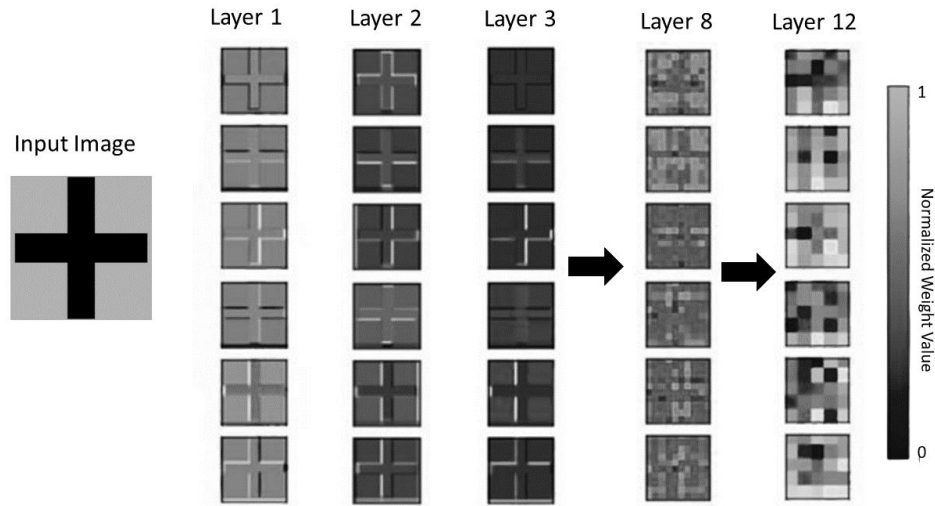


Figure 5.7: Features maps in fully connected layers

5.2. Model Details and Learnable Parameters

The input layer only reads the images so, it has zero learnable parameters. The pooling layer also doesn't have any learnable parameters as only image dimensional size is changed in this layer. In convolutional, fully connected layers the output nodes have separate weights and additional nodes applied so, the learnable parameters are given by $n \cdot m \cdot k \dots k_1$ and $(n + 1) \cdot m$ parameters respectively. The output layer is fully connected so it's represented by the same fully connected learnable parameters. The dimensionality of the first fully connected layer is unknown so, it is given by $input\ size - (filter\ size - 1)$ parameters. To calculate the number of parameters the network learned $(n \cdot m \cdot k + 1) \cdot f$

Different CNN architectures generate different feature map responses in corresponding layers and result in different validations, accuracy, root mean squared error (RMSE), and training time. Nine models were used with different architectures to find out the best hyperparameters that gives low mean square error. The stochastic gradient descent model (SGDM) was used to train and calculate metrics over certain epochs taking steps in every batch and keeping track of the metrics on each epoch as well as the overall best metrics in models 1-3. Table 5-1 shows details about models.

Model 1-3 consists of three stacked convolutional layers each consisting of a batch normalization layer, ReLU and leakyReLU activation layer, and max-pooling layer. The CNN

models employed 3x3 filters in each convolutional layer, with 8, 16, 32, 64, and 128 filters in the successive layers. The pooling layer comprised of 2x2 windows dragging across the input feature map with the same (full) padding and stride of 2. Model 2-6 consists of four stacked architectures and model 7-9 consists of five stacked layers respectively trained with the adaptive moment estimation algorithm (ADAM). Additionally, during the training process, a learning rate of 0.001 was utilized along with a β_1 value of 0.9 and a β_2 value of 0.99. A test dataset consisting of 10% of the overall data was also used.

5.3. Black Box Opening and Model Prediction

To gain insights into CNN's predictions and open the black box of the best-performing model, the Deep SHapley Additive Explanations (SHAP) framework was used. The framework is derived from game theory which gives unified explanations. Deep SHAP incorporates DeepLIFT, a technique that was previously used to split predictions of outputs using Shapley values with backpropagation. These values are a measure employed to determine feature significance to generate heatmap-based explanations at the pixel level and express the contribution of each feature in generating the absorption spectra. The explanations generated by Deep SHAP shows that the CNN has picked up on key physical characteristics of metamaterials group under investigation, such as the relationships between structural components and optical outputs for basic and complex resonator topologies. So, the method is useful in determining specific geometric contributions to machine learning predictions of nanophotonic device properties, allowing a better understanding of the behavior of complex nanophotonic devices and identifying pathways to improving their designs. The shap values are calculated by SHAP algorithm is expressed as:

$$\Phi_i(f, x) = \sum_{z' \subseteq x'} \frac{|z'|! (m - |z'| - 1)!}{m!} \left[f_x(z') - f_x\left(\frac{z'}{i}\right) \right] \quad (5.10)$$

where, Φ_i represents the shap values, m represents the number of input features, x' represents the binary values of input space (x), z' represents non-zero indices in binary values x' . The model trained with z' is given by the expression $f_x(z')$. The heatmaps are presented in the next chapter.

Table 5-1: Layers, Parameters of trained CNN architectures

Model 1			Model 2			Model 3		
Layer	Parameter	Option	Layer	Parameter	Option	Layer	Parameter	Option
2D-conv. ReLU MaxPool	3x3, 16 2x2, s=2	SGDM Batch=16	2D-conv. ReLU MaxPool	3x3, 32 2x2, s=2	SGDM Batch=16	2D-conv. leakyReLU MaxPool	3x3, 32 2x2, s=2	SGDM Batch=16
2D-conv. ReLU MaxPool	3x3, 32 2x2, s=2	Epoch= 315 (ES)	2D-conv. ReLU MaxPool	3x3, 32 2x2, s=2	Epoch= 235	2D-conv. leakyReLU MaxPool	3x3, 32 2x2, s= 2	Epoch= 221
2D-conv. ReLU	3x3, 64		2D-conv. ReLU	64 3x3,		2D-conv. leakyReLU	3x3, 64	
Model 4			Model 5			Model 6		
Layer	Parameter	Options	Layer	Parameter	Options	Layer	Parameter	Option
2D-conv. ReLU Avg Pool	3x3, 8 2x2, s=2	ADAM Batch=16	2D-conv. ReLU MaxPool	3x3, 16 2x2, s=2	Batch=16 Epoch= 308	2D-conv. leakyReLU MaxPool	3x3, 16 2x2, s=2	Batch=16 Epoch= 320
2D-conv. ReLU AvgPool	3x3, 16 2x2, s= 2	Epoch= 332	2D-conv. ReLU MaxPool	3x3, 32 2x2, s=2		2D-conv. leakyReLU MaxPool	3x3, 32 2x2, s=2	
2D-conv. ReLU AvgPool	3x3, 32 2x2, s=2		2D-conv. ReLU AvgPool	3x3, 32 2x2, s=2		2D-conv. leakyReLU MaxPool	3x3, 32 2x2, s=2	
2D-conv. ReLU	3x3, 32		2D-conv. ReLU	3x3, 64		2D-conv. leakyReLU	3x3, 64	
Model 7			Model 8			Model 9		
Layer	Parameter	Option	Layer	Parameter	Option	Layer	Parameter	Option
2D-conv. ReLU Avg Pool	3x3, 8 2x2, s=2	Batch=16 Epoch= 300	2D-conv. ReLU Avg Pool	3x3, 8 2x2, s=2	Batch=16 Epoch= 300	2D-conv. ReLU Avg Pool	3x3, 8 2x2, s=2	Batch=16 Epoch= 300
2D-conv. ReLU AvgPool	3x3, 16 2x2, s= 2		2D-conv. ReLU AvgPool	3x3, 16 2x2, s= 2		2D-conv. ReLU AvgPool	3x3, 16 2x2, s= 2	
2D-conv. ReLU AvgPool	3x3, 32 2x2, s=2		2D-conv. ReLU AvgPool	3x3, 32 2x2, s=2		2D-conv. leakyReLU AvgPool	3x3, 32 2x2, s=2	
2D-conv. ReLU AvgPool	3x3, 32 2x2, s=2		2D-conv. ReLU AvgPool	3x3, 64 2x2, s=2		2D-conv. leakyReLU AvgPool	3x3, 64 2x2, s=2	
2D-conv. ReLU AvgPool	3x3, 64 2x2, s=2		2D-conv. ReLU AvgPool	3x3, 128 2x2, s=2		2D-conv. leakyReLU AvgPool	3x3, 128 2x2, s=2	

Chapter 6:

Results and Discussion

This chapter focuses on the results and discussions of FDTD simulations, model architecture, best-performing hyperparameter, set-up, material properties, and design of nanophotonic metamaterials.

6.1. FDTD Results Based on Resonator Shape

The simulation results provide an understanding of the flow of energy between the resonator (ZnO) and the substrate (perovskite) layer. The absorption of energy in a resonator and active layer substrate is influenced by factors such as the resonant frequency, the resonator shape, size, and the surrounding medium's dielectric properties. The results were obtained by plotting the time-domain response of the resonator.

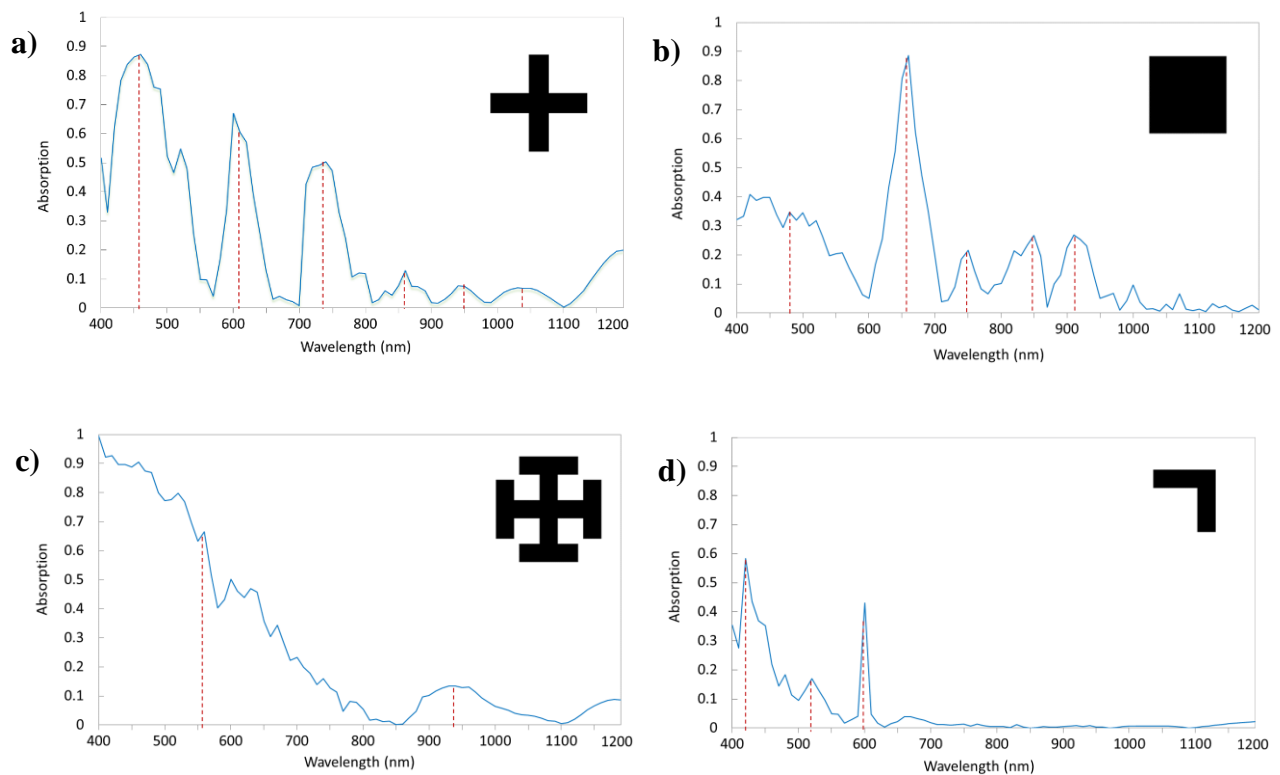


Figure 6.1: Absorption spectrum of resonator w.r.t different shapes

Fig 6.1 (a) shows cross-shape resonators ($L_1=3000\text{nm}$ and $L_2=500\text{nm}$ width) display 6-8 different absorption peaks in different wavelength regions among them the ones at 450nm , 600nm , and 750nm reached the absorption efficiency above 70% . (b) shows square resonators display 3 diffused peaks ranging from $400\text{-}900\text{nm}$ and a sharp peak at 660nm with 87% absorption in this region. (c) shows window-shaped resonators display high resonance resulting in a single diffused absorption peak from a range $400\text{-}800\text{nm}$ with $70\text{-}96\%$ absorption till 500nm and $10\text{-}50\%$ absorption in $600\text{-}800\text{nm}$ window. (d) shows the absorption spectrum of an L-shaped resonator.

6.2. FDTD Results Based on Resonator Size

The absorption of energy in the nanostructured active layer increased as the size of the resonator increased from 100nm to 3500nm . The peaks shifted from high to low energy wavelength as the Length (L_1) and width (L_2) of the resonator increased. Figure 6.2 a), b), and c) shows the total absorption spectra of the cross-shaped, window-shaped, and square resonators of three incremental increasing sizes (500 , 1500 , and 2500nm) respectively.

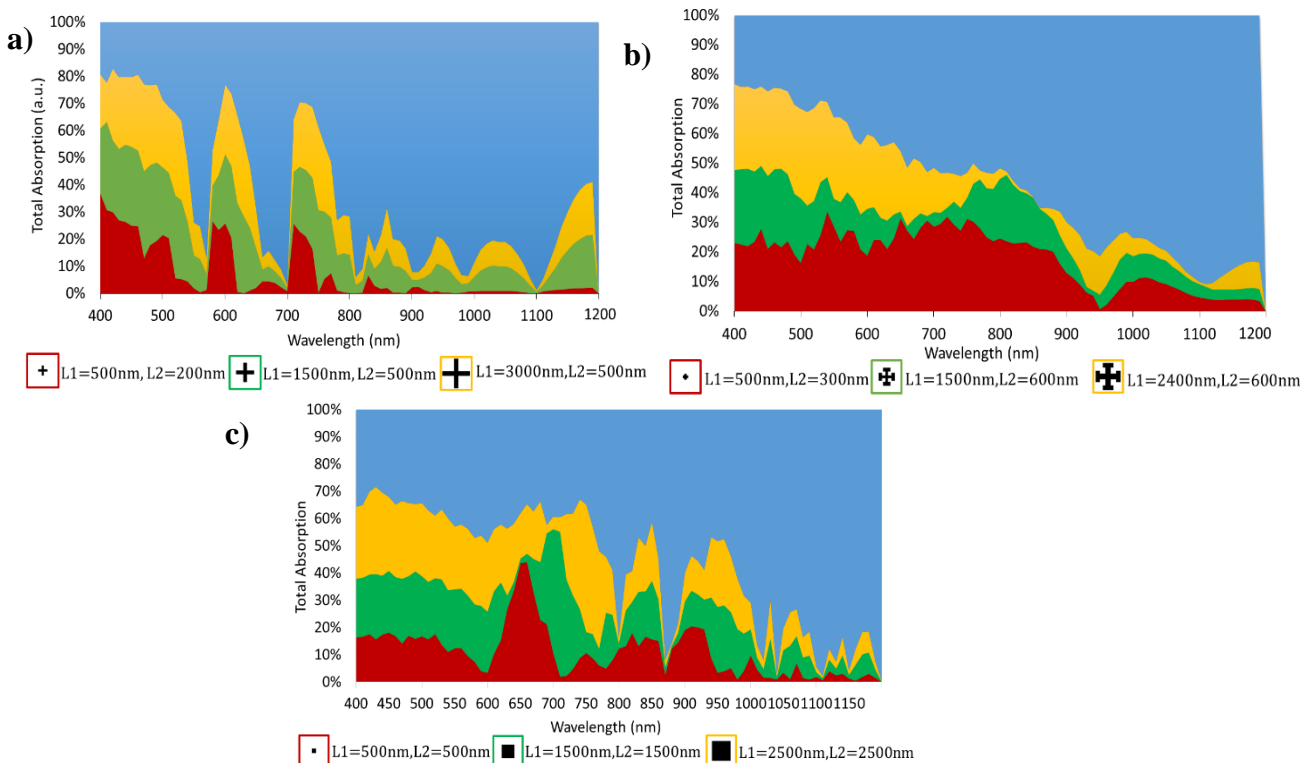


Figure 6.2: Absorption spectrum of resonator w.r.t different sizes

6.3. CNN- Forward Propagation Results

All the CNN models successfully performed forward propagation of resonator design with low error values. As shown in table 6.1, Model 1-3, (3-layered stacked CNN) had the highest RMSE values which indicates that the ADAM optimizer performed well than the SGDM as it reduced the RMSE by 10x. Model 9 performed exceptionally well with the least error (RMSE=0.00375) and a validation accuracy of 68%. Figure 6.5. a) depicts the loss function of Model 9's validation and training phases over increasing epochs as a graph b) shows the graph of loss function of training and validation accuracy of the model. The training loss and accuracy graphs of Model 1-8 are given in Appendix A).

Table 6-1: Outcomes of trained CNN with the associated RMSE values, validation accuracy, and training time

CNN Model	RMSE	Validation Accuracy	Training Time
Model 1	0.069	0.407	10m 19s
Model 2	0.0264	0.416	13m40s
Model 3	0.016	0.4593	14m20s
Model 4	0.0086	0.4488	15m20s
Model 5	0.0045	0.4488	15m
Model 6	0.00528	0.4734	14m26s
Model 7	0.00449	0.5390	8m8s
Model 8	0.00449	0.5390	23m6s
Model 9	0.00375	0.6847	23m

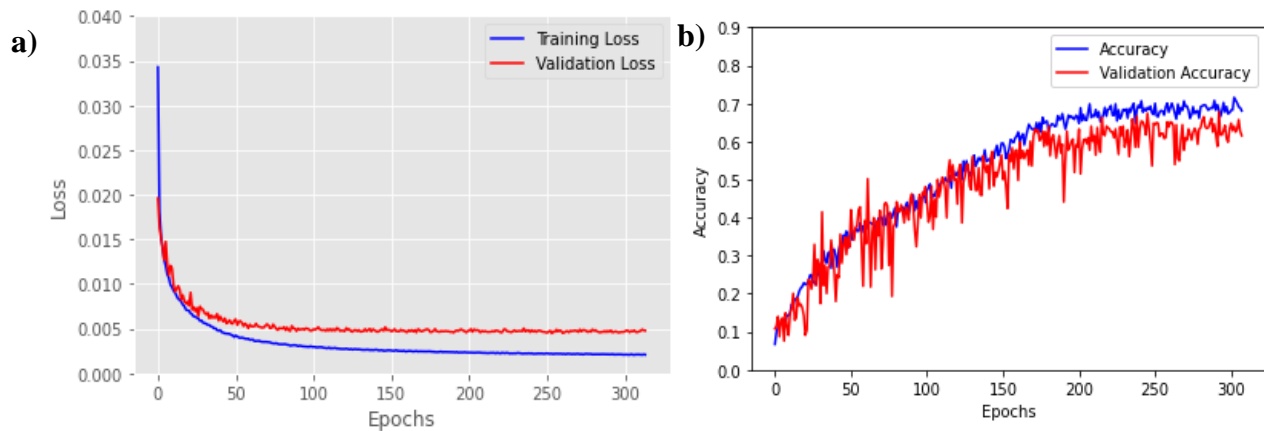


Figure 6.3: Training Graphs showing a) CNN Model-9 Training and Validation Loss b) CNN Model-9 Training and Validation Accuracy

6.4. Prediction Results

The prediction results were obtained by comparison of the mean absolute accuracy of the CNN prediction spectrum and simulations. The results show that CNN shows high prediction accuracy of resonator geometry aside from the training dataset. The predicted absorption peaks display a wavelength and amplitude that closely match those of the simulated peaks. Some minor variations were observed in the intensity and regions outside of the peaks when compared to simulated results. The CNN-based predictions were generated much faster, taking an average of 0.3 ± 0.05 seconds per prediction, whereas each FDTD simulation ($n=9$) took approximately 25 minutes hence, the CNN is 85 times faster than conventional solvers. The prediction results highlight the successful performance of CNN in accomplishing the forward propagation and resonator design task of TSC with a high level of accuracy. The structure analysis of resonator depicts that CNN has learned the ML-inspired physical relationship. The filters can be optimized further so, the mean absolute accuracy can be enhanced when comparing CNN's prediction to the FDTD absorption spectra of the given resonator shape.

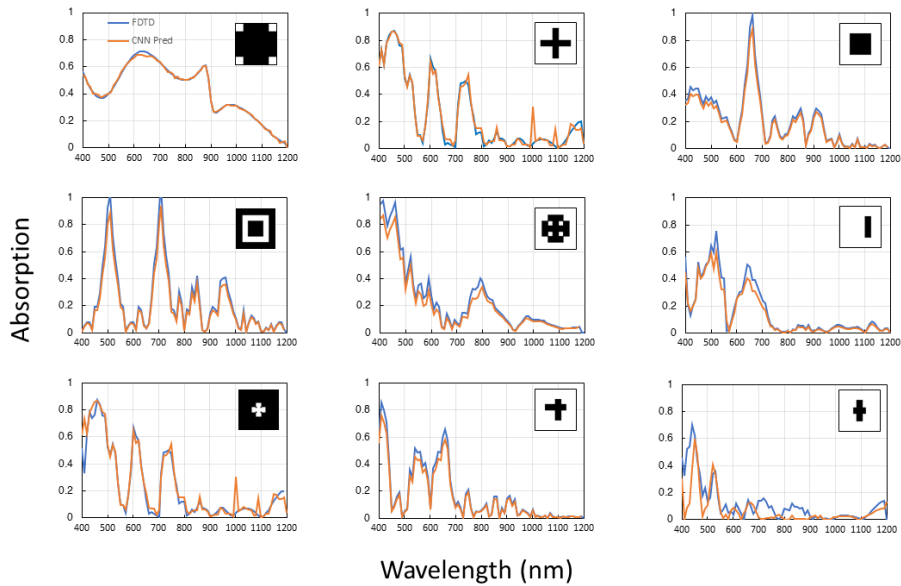


Figure 6.4: CNN Prediction and FDTD simulation of the 9-different resonator of the training dataset

6.5. DeepShap Results

The SHAP algorithm utilizes a selection of background samples to approximate the dependent targets of SHAP values in deep learning models. Even when a feature is missing, the method can nevertheless estimate its effect on the model output by substituting values from the backdrop. So, a white background was used to reduce the noise in the results.

6.5.1. SHAP Explanations:

A heatmap is used to illustrate the SHAP explanation, with red pixels indicating positive contributions of the base image towards the model's prediction, and blue pixels indicating negative contributions as shown in Figure 6.5. The SHAP values were captured at wavelengths 450, 650, 850, 1050, and 1200nm with a single reference white background. The base images were resonators having 80-point absorption peaks.

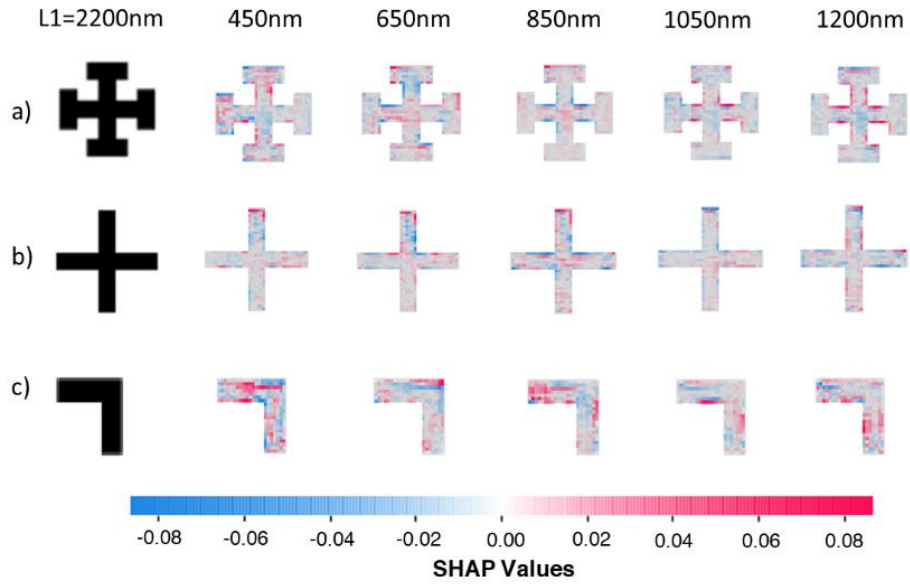


Figure 6.5: SHAP CNN Explanations of metasurfaces (L1=2200nm, L2=300nm) Predictions at increasing wavelengths a) Window resonator b) Cross resonator c) L-arm resonator

6.5.2. SHAP Cross-arm validation

DeepSHAP depicts regions of pixels that travel from the centre of the base representation to its edges as the wavelength rises. This shows that to obtain resonance at longer wavelengths, the arm dimensions must be increased.

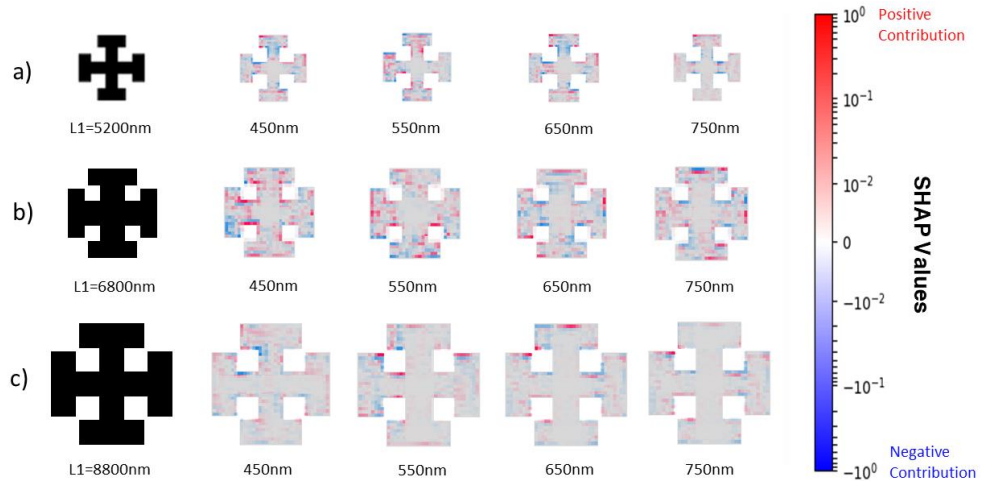


Figure 6.6: SHAP CNN Validation at 450-800nm of a) L1=5200nm, L2=300nm b) L1 6800nm, L2= 500nm c) 8800nm, L2=700nm

The validation method helps identify the relationship between geometric structures and optical responses of every pixel embedded in the feature map. The diffused absorption and sharp peak resonance behaviors were studied to suppress the negative contributing pixels in the range of 600-800nm. Figure 6.7. provide examples of validation where the explanations of a sharp-peaked structure (cross-shaped) and a diffused absorption peaked resonator (window-shaped) were recorded at the peak wavelengths as pointed out in 6.7(a). The explanation heat maps are shown from wavelength 450-800nm in 6.7(b). The target is to replace the negative contributing pixel response with the positive pixels to obtain maximum absorption in the region. Figures 6.7 (c) and (d) represent the target wavelength of the cross-base image as well as the explanations for cross-base imaging at respective wavelengths. The red dashed box represents the validated structure leading to the highest contribution to maximum absorption in the region while the blue dashed box represents the highest negative contribution.

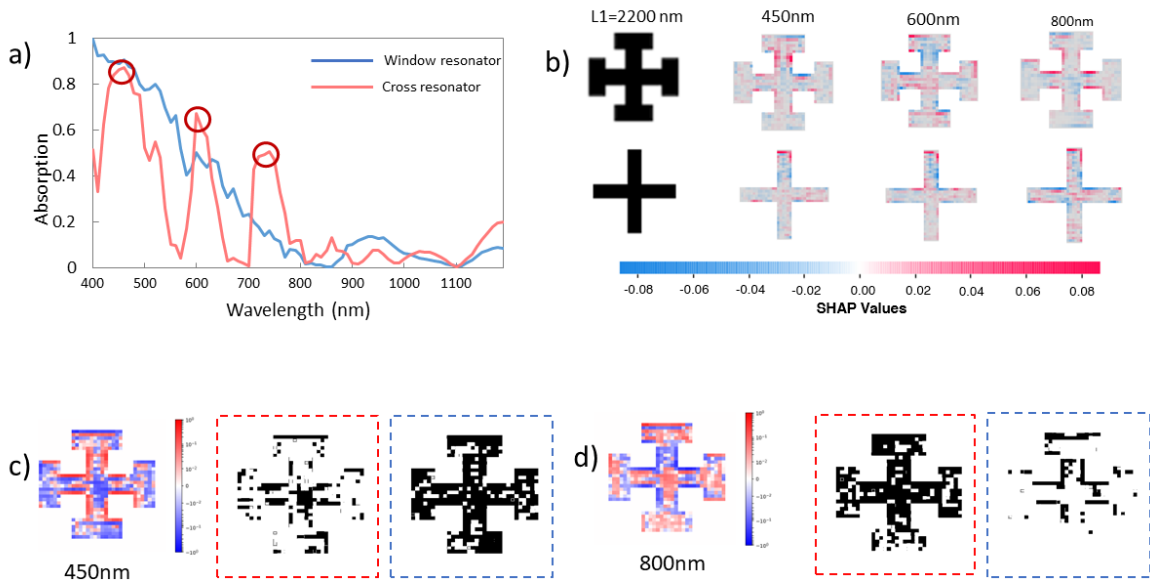


Figure 6.7: SHAP CNN Validation a) Absorption peaks of window and cross resonator at L1=2200nm b) SHAP explanations of the resonators at wavelength 450-800nm c), d) SHAP explanation of the validated cross-window base image at 600-800nm

Figure 6.8. shows average SHAP validation values of the SHAP explanation at given wavelenths. A) represents the SHAP validation curves in graph 6.8 (a), (b), (c), and (d) represent

the target and base curves at 450, 600, 700, and 800nm respectively. The graphs show the highest negative SHAP values (blue pixels) have higher proportions which need to be replaced by contributing pixels in that specific wavelength. However, figure 6.8 (d) More negative maximum SHAP values (blue cells) are produced at 700–800 nm than at diffused–peak wavelengths according to SHAP explanations. The present results demonstrate that the presence of sharp absorption peaks at 600 and 750 nm is determined by the CNN by including the horizontal and vertical bars on the cross-resonator.

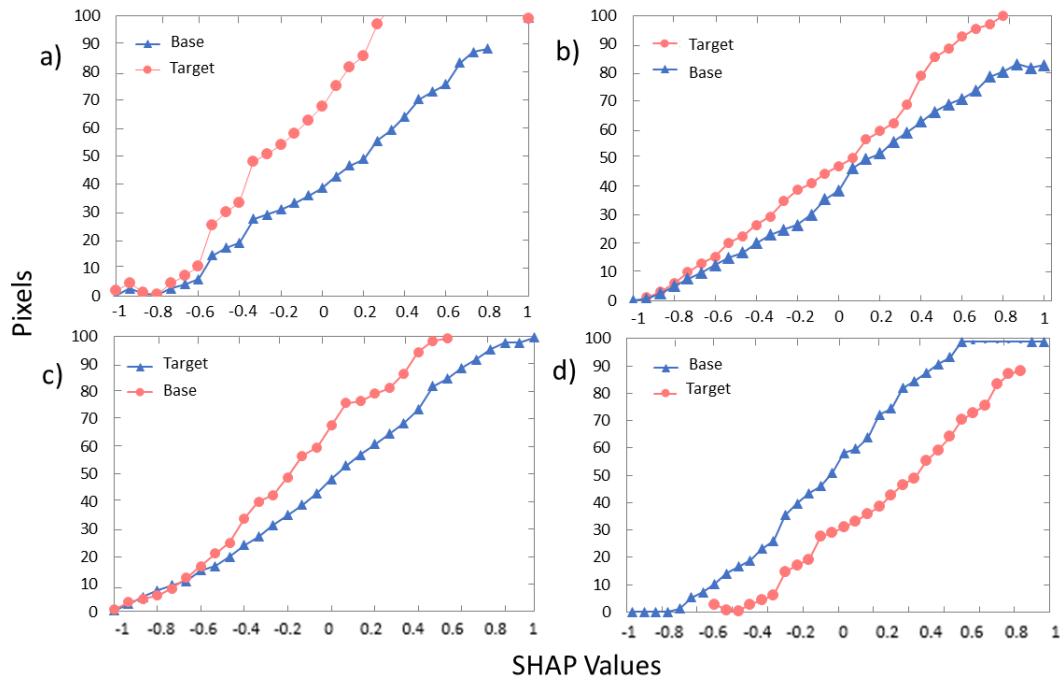


Figure 6.8: Average SHAP validation values of SHAP explanation a) 450nm b) 600nm c) 700nm d) 800nm

The design's validation studies show how translating the pixels from the feature maps identified by the SHAP heat maps can help achieve complex spectral targets. As a result, the heatmaps themselves shed light on the relationship between geometric properties and EM response. The low-intensity diffused peak structure at 600-800nm was converted into a well-defined peak structure by restricting the picture conversion procedure to the photons of a certain target wavelength.

The SHAP explanations offer detailed insights into the specific regions of each resonator that contribute to individual resonance peaks. For example, for the sharp peaks in cross-shaped

structure, the explanation at each peak (600 nm and 700 nm) shows various regions that are dominated by red pixels. The spatial distribution of the heatmap is closely related to the spatial properties of the resonances on each peak. Particularly, at various resonance wavelengths, the electric field intensities within the structures vary. The resonance at different wavelength and electric field profiles are given in Figures 6.9 and 6.10.

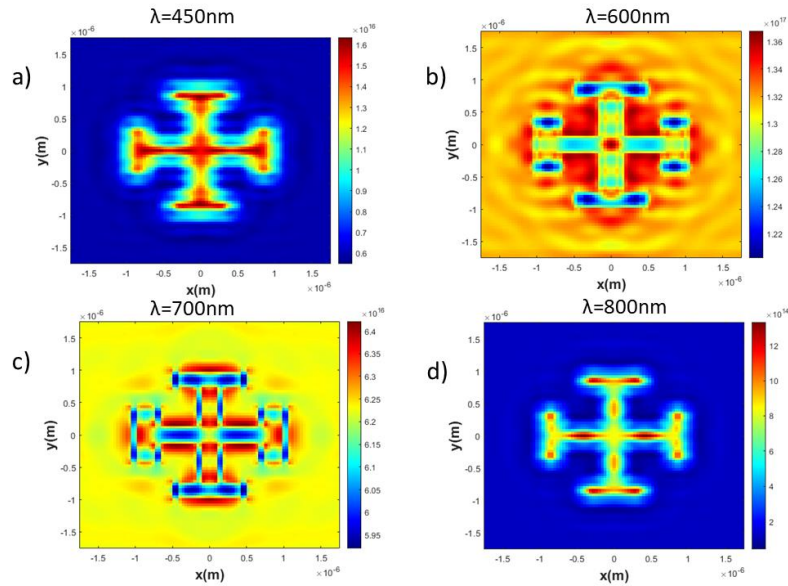


Figure 6.9: Resonance Profile of SHAP Validated Structures a) 450nm b) 600nm c) 700nm d) 800nm

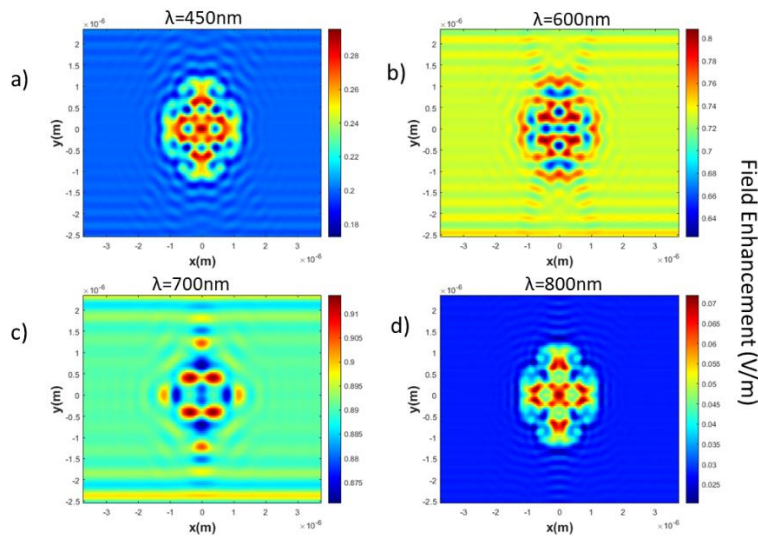


Figure 6.10: Electric field Profile of SHAP Validated Structures a) 450nm b) 600nm c) 700nm d) 800nm

6.6. Solar Cells Absorption Result

The validated metasurface designs were integrated with the Si bottom sub-cell to evaluate the optical performance of the TSC. The absorption plots evaluate the solar cell performance and display the optical losses in the various layers and cells at specific wavelengths. To compare the improvement in light absorption in perovskite/Si TSC, the typical reference TSC architecture was compared with metasurfaces integrated-TSC. Figure 6.11 (a) shows the optical absorption in reference 2T- perovskite top and Si bottom cells without any top metasurface cell along with other conducting layers like TCO, and ZnO. The active layer comprises of near 90% absorption of the solar spectrum. The estimated J_{sc} of the top and bottom cells is $17.5\text{mA}/\text{cm}^2$ and $20\text{mA}/\text{cm}^2$ respectively. There are significant optical losses in the Ultraviolet (UV) and NIR regions. These losses may be due to parasitic or reflective losses.

Figure 6.11 (b) shows the optical absorption in 2T- perovskite metasurface and Si bottom cell. The average absorption of the top cell increased in the UV-vis region (650-800nm) up to 93.4%. The bandwidth of absorption in the Si bottom cell also increased which shows that the metasurface transmits or scatters the unabsorbed NIR light to the bottom cell. The active layer comprises of near 92% absorption of the solar spectrum. The estimated J_{sc} of the top and bottom cells is $19.5\text{mA}/\text{cm}^2$ and $20\text{mA}/\text{cm}^2$ respectively. The J_{sc} in the top cell increased by $2\text{mA}/\text{cm}^2$ by integrating the optimized metasurface with the bottom cell. This increase is due to enhanced light trapping, resonance, and electromagnetic response because of the designed metasurface. The optical losses have also decreased as compared to the reference TSC architecture. The absorption in the TCO layer also increased by 10%. The rest of the optical losses are mainly parasitic and interface losses which can be reduced by introducing an interlayer or modifying the absorber layer thickness. The recorded V_{oc} of the TSC is 0.7397V. The total J_{sc} of $35.91\text{ mA}/\text{cm}^2$. The fill factor observed is 82.2% with eta 21.84%.

The absorption curves were also plotted alongside the spectral irradiance AM 1.5 graph. Figure 6.12 shows the optical absorption in 2T- perovskite/Si TSC. For reference, the AM 1.5 solar irradiance curves are represented in the black curve. The red portion displays the energy absorbed by the solar cell while the blue portion represents the unabsorbed spectrum.

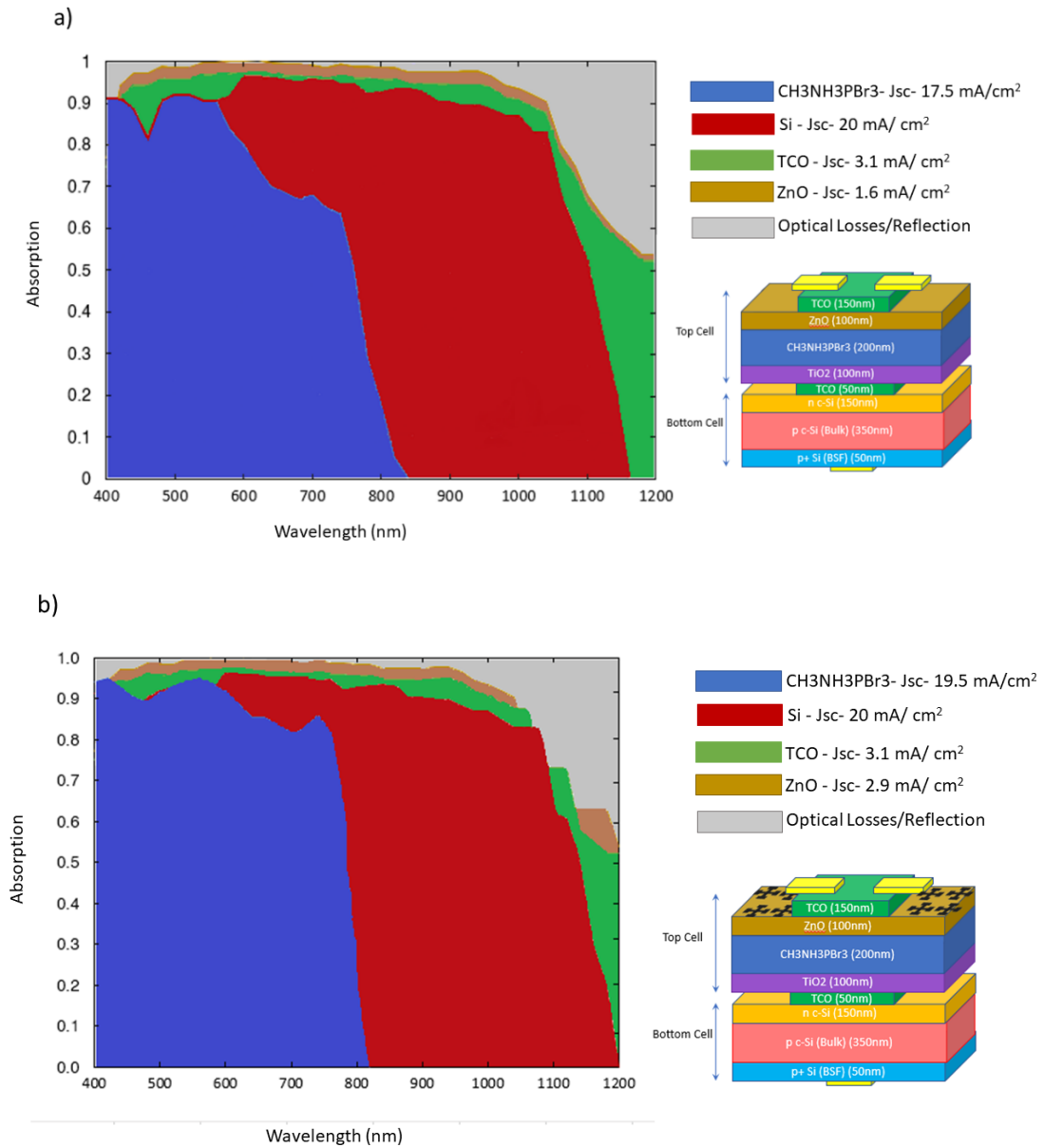


Figure 6.11: Optical absorption in 2T-perovskite/Si TSC (a) reference configuration without metasurface (b) configuration with integrated metasurface top cell

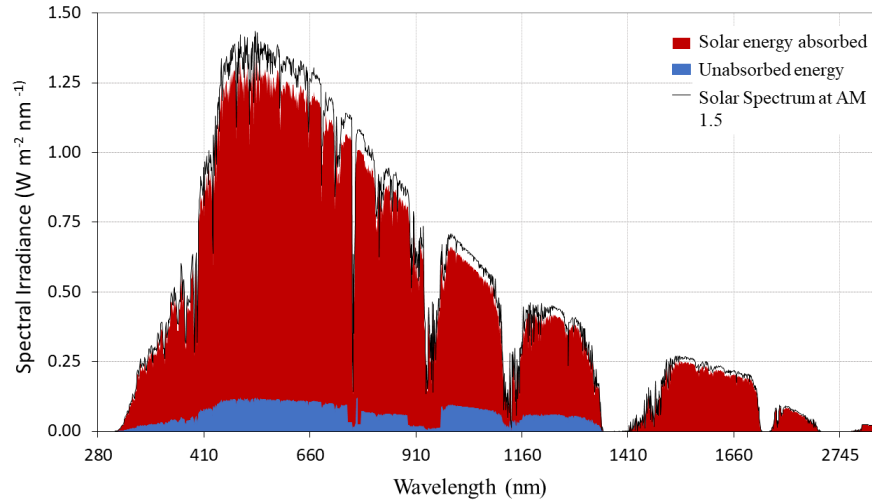


Figure 6.12: Optical absorption in 2T- perovskite/Si TSC (integrated metasurface) with reference to the AM 1.5 irradiance spectrum

6.7. Generation Rate and External Quantum Efficiency

J_{sc} achieves considering only the optical properties of the solar cell architecture, disregarding non-ideal effects on the transport and extraction of charge carriers. The G parameter may be represented in 1D or 2D profiles as a function of position and/or incoming light wavelength values. Figures 6.13 show the generation rate of 2T- perovskite/Si TSC (integrated metasurface).

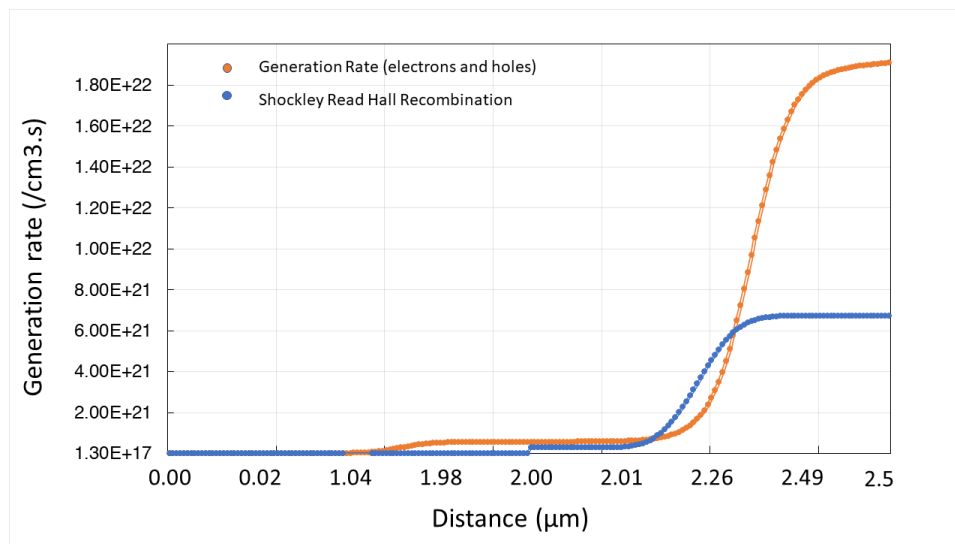


Figure 6.13: Carrier Generation rate profile in 2T- perovskite/Si TSC (integrated metasurface)

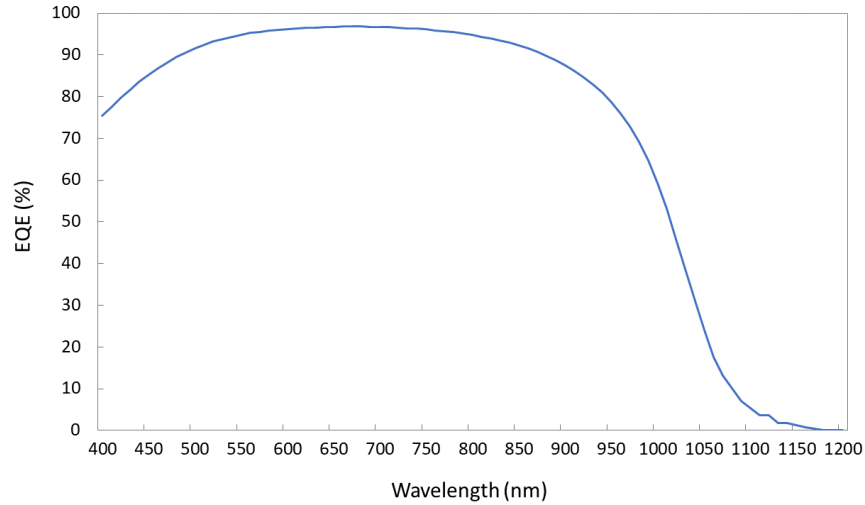


Figure 6.14: EQE in 2T- perovskite/Si TSC (integrated metasurface)

The use of deep learning for optimizing metasurfaces in TSC has yielded promising results in terms of EQE and current density. As this approach is relatively new and not yet widely adopted, direct comparison with similar studies is challenging. Nonetheless, the use of metasurfaces for light management in TSC has been explored in various research, and the current design was compared with recent studies, as seen in Table 6-2.

Table 6-2: Comparison of the state-of-the-art Metasurface with recent studies and findings

Study	Solar Cell	Metasurface	Absorption	Jsc(metasurface)/EQE
[42]	2T-Hybrid organic-inorganic perovskite TSC	Nanohole array-Mie Resonant Metasurface	>90% in wavelength (400-770nm)	65.2% EQE
[41]	4T- perovskite/Si TSC	Mie Resonant spectrum splitting Metasurface	92% in wavelength (400-800nm)	22.1 mA/cm ² of top perovskite cell
[22]	2T- perovskite/Si TSC	Dielectric Hybrid Metasurface	Low reflectivity in UV-vis region (<15%)	19.55 mA/cm ² of top perovskite cell
Current	2T- perovskite/Si TSC	Dielectric Hybrid Metasurface	>90% in wavelength (400-800nm)	19.5 mA/cm ² of top perovskite cell 87% EQE

Conclusion

In this study, the use of deep learning to predict the optimal optical design for the top cell, maximizing PCE, and the effect of metasurfaces on solar cell architecture were studied. The metasurfaces proposed in this study include three stacked layers. Several computational techniques have been developed to analyze the optical responses of metasurfaces in solar cells, which are essential as experimental techniques often use a costly and time-consuming trial-and-error approach given the many parameters involved. The use of learning-based optimization using CNN is an effective data-driven approach to solving complex non-linear optical problems and predicting the design space by identifying the best input and unidentified regions with previous information.

A dataset consisting of 10,578 $\text{TiO}_2/\text{MAPBI}_3/\text{ZnO}$ metasurfaces was used. 3-D FDTD by ANSYS Lumerical v202 was used for simulations. The resonator was a cross, square, L-shaped, window-shaped polygon and its inverted version. The shapes were chosen because of the ease of fabrication by the lithography technique. The FDTD results display that cross-shape resonators ($L_1=3000\text{nm}$ and $L_2=500\text{nm}$ width) display 6-8 different absorption peaks in different wavelength regions among them the ones at 450nm, 600nm, and 750 nm reached the absorption efficiency above 70%. square resonators display 3 diffused peaks ranging from 400-900 nm and a sharp peak at 660nm with 87% absorption in this region. Several CNN architectures were used to find the best hyperparameters that give the low mean square error, and the stochastic gradient descent model (SGDM) was used to train and calculate metrics over certain epochs, taking steps in every batch and keeping track of the metrics on each epoch, as well as the overall best metrics in models 1-3. Model 2-6 consists of four stacked architectures, and model 7-9 consists of five stacked layers respectively trained with the adaptive moment estimation algorithm (ADAM). A test dataset consisting of 10% of the overall data was also used.

The results showed that the proposed SHAP framework can be used to gain insights into CNN's predictions and open the black box of the best-performing model. The framework is derived from game theory, which gives unified explanations. Deep SHAP integrates DeepLIFT and Shapley values. These values are a measure employed to determine feature significance to generate heatmap-based explanations at the pixel level and express the contribution of each feature

in generating the absorption spectra. Deep SHAP shows that CNN has picked up on key physical characteristics of the metamaterials group under investigation, such as the relationships between structural components and optical outputs for elementary and complex resonator geometries. The prediction results were obtained by comparison of the mean absolute accuracy of the CNN prediction spectrum and simulations. The results show that CNN shows high prediction accuracy of resonator geometry aside from the training dataset. The CNN-based predictions were generated much faster, taking an average of 0.3 ± 0.05 seconds per prediction, whereas each FDTD simulation ($n=9$) took approximately 25 minutes hence, the CNN is 85 times faster than conventional solvers. The prediction results highlight the successful performance of CNN in accomplishing the forward propagation and resonator design task of TSC with a high level of accuracy.

The SHAP-validated metasurfaces designs were integrated with the Si bottom sub-cell to evaluate the optical capabilities of the TSC in SCAPS-1D. The active layer comprises of near 90% absorption of the solar spectrum. The average absorption of the top (metasurface-integrated) cell increased in the UV-vis region (650-800nm) up to 93.4%. The bandwidth of absorption in the Si bottom cell also increased which shows that the metasurface transmits or scatters the unabsorbed NIR light to the bottom cell. The estimated J_{sc} of the top and bottom cells is $19.5\text{mA}/\text{cm}^2$ and $20\text{mA}/\text{cm}^2$ respectively. The J_{sc} in the top cell increased by $2\text{mA}/\text{cm}^2$ by integrating the optimized metasurface with the bottom cell. The recorded V_{oc} of the solar cell is 0.7397V . The total J_{sc} of $35.91\text{ mA}/\text{cm}^2$. The fill factor observed is 82.2%.

Overall, the study provides significant insights into the use of deep learning and metasurfaces in solar cell architecture. A better understanding of the behavior of complicated nanophotonic devices and the identification of avenues for enhancing their designs are made possible by the suggested method, which is effective in detecting specific geometric inputs to machine learning predictions of nanophotonic device features. The use of learning-based optimization using 2D-CNN and the proposed SHAP-framework can help reduce the cost and time required for trial-and-error methods and give a more thorough grasp of the functioning of sophisticated nanophotonic devices. This study provides an important step forward in the development of efficient, cost-effective, and environmentally friendly solar cell technology.

Research Gaps

The optimization studies can now yield better information regarding the need for nanoscale structures for better light management and predict better design space to enhance PCE. The active layer can itself be used as light managing, directing, and restricting layers or metasurfaces. However, there are several opportunities and questions untapped in the realm of optical optimization. An extensive optimization space is needed to compute different parameters at the same time such as refractive index, band gap, donor/acceptor concentration ratio, fill factor, and internal morphologies to grasp a better understanding of active layer optimization for fabrication of lattice and current matched TSC to enhance its PCE [67]. When the gratings are periodically simulated in 2D, the processing needs of boundary value issues grow dramatically. Multiple design parameters introduced into the optimization process increase the computational load even further. As textured TSC simulation also takes a long time, the amount of free space design parameters is also limited. The choice of parameters needs to be made based on the optical performance of varying layers and thicknesses. So, only the length, width, and arm lengths of the resonator were considered for the study.

Prospects

In the future, this study can be improved. Generic 2D-CNN architecture (with 3–5-layer stacks) were trained for this study. Several other advanced Neural Network architectures can be studied for optimizing the TSCs. GANs, AlexNet, GoogLeNet, Federated Learning, and ResNet can also be used for the optical optimization of TSCs. The current study only used 2D images and 1 channel as input. Color-encoded (RGB) 3D images can also be used which can represent the range of material and structural parameters, and geometric design. Furthermore, more parameters can be considered for optical design and optimization like Materials search, thickness, texturization, etc.

References

- [1] A. Hepbasli, “A key review on exergetic analysis and assessment of renewable energy resources for a sustainable future,” *Renew. Sustain. Energy Rev.*, vol. 12, no. 3, pp. 593–661, 2008, doi: <https://doi.org/10.1016/j.rser.2006.10.001>.
- [2] K. Yoshikawa *et al.*, “Silicon heterojunction solar cell with interdigitated back contacts for a photoconversion efficiency over 26%,” *NatEn*, vol. 2, no. 5, p. 17032, Mar. 2017, doi: [10.1038/NENERGY.2017.32](https://doi.org/10.1038/NENERGY.2017.32).
- [3] W. Shockley and H. J. Queisser, “Detailed balance limit of efficiency of p-n junction solar cells,” *J. Appl. Phys.*, vol. 32, no. 3, pp. 510–519, Mar. 1961, doi: [10.1063/1.1736034](https://doi.org/10.1063/1.1736034).
- [4] S. Rühle, “Tabulated values of the Shockley-Queisser limit for single junction solar cells,” *Sol. Energy*, vol. 130, pp. 139–147, Jun. 2016, doi: [10.1016/j.solener.2016.02.015](https://doi.org/10.1016/j.solener.2016.02.015).
- [5] A. Polman, M. Knight, E. C. Garnett, B. Ehrler, and W. C. Sinke, “Photovoltaic materials: Present efficiencies and future challenges,” *Science*, vol. 352, no. 6283. American Association for the Advancement of Science, Apr. 15, 2016. doi: [10.1126/science.aad4424](https://doi.org/10.1126/science.aad4424).
- [6] Z. Yu, M. Leilaieoun, and Z. Holman, “Selecting tandem partners for silicon solar cells,” *Nature Energy*, vol. 1, no. 11. Nature Publishing Group, pp. 1–4, Sep. 19, 2016. doi: [10.1038/nenergy.2016.137](https://doi.org/10.1038/nenergy.2016.137).
- [7] G. E. Eperon, M. T. Hörantner, and H. J. Snaith, “Metal halide perovskite tandem and multiple-junction photovoltaics,” *Nat. Rev. Chem.*, vol. 1, no. 12, pp. 1–18, Dec. 2017, doi: [10.1038/s41570-017-0095](https://doi.org/10.1038/s41570-017-0095).
- [8] J. P. Mailoa *et al.*, “A 2-terminal perovskite/silicon multijunction solar cell enabled by a silicon tunnel junction,” *Appl. Phys. Lett.*, vol. 106, no. 12, p. 121105, Mar. 2015, doi: [10.1063/1.4914179](https://doi.org/10.1063/1.4914179).
- [9] Y. Wu *et al.*, “Monolithic perovskite/silicon-homojunction tandem solar cell with over 22% efficiency,” *Energy Environ. Sci.*, vol. 10, no. 11, pp. 2472–2479, Nov. 2017, doi: [10.1039/c7ee02288c](https://doi.org/10.1039/c7ee02288c).
- [10] K. J. Kim, C. U., Yu, J. C., Jung, E. D., Choi, I. Y., Park, W., Lee, H., & Choi, “Optimization of device design for low cost and high efficiency planar monolithic perovskite/silicon tandem solar cells,” *Nano Energy*, vol. 60, pp. 213–221, 2019.
- [11] D. Grant, K. Catchpole, K. Weber, and T. White, “Design guidelines for perovskite/silicon 2-terminal tandem solar cells: An optical study,” *Opt. Express*, vol. 24, pp. A1454–A1470, 2016, doi: [10.1364/OE.24.0A1454](https://doi.org/10.1364/OE.24.0A1454).
- [12] Y. Jiang *et al.*, “Optical analysis of perovskite/silicon tandem solar cells,” *J. Mater. Chem.*

- C, vol. 4, no. 24, pp. 5679–5689, Jun. 2016, doi: 10.1039/C6TC01276K.
- [13] F. Sahli *et al.*, “Improved Optics in Monolithic Perovskite/Silicon Tandem Solar Cells with a Nanocrystalline Silicon Recombination Junction,” *Adv. Energy Mater.*, vol. 8, no. 6, p. 1701609, Feb. 2018, doi: 10.1002/AENM.201701609.
- [14] F. Sahli *et al.*, “Fully textured monolithic perovskite/silicon tandem solar cells with 25.2% power conversion efficiency,” *Nat. Mater.* 2018 179, vol. 17, no. 9, pp. 820–826, Jun. 2018, doi: 10.1038/s41563-018-0115-4.
- [15] L. Mazzarella *et al.*, “Infrared Light Management Using a Nanocrystalline Silicon Oxide Interlayer in Monolithic Perovskite/Silicon Heterojunction Tandem Solar Cells with Efficiency above 25%,” *Adv. Energy Mater.*, vol. 9, no. 14, p. 1803241, Apr. 2019, doi: 10.1002/AENM.201803241.
- [16] L. Mazzarella *et al.*, “Infrared photocurrent management in monolithic perovskite/silicon heterojunction tandem solar cells by using a nanocrystalline silicon oxide interlayer,” *Opt. Express*, vol. 26, 2018, doi: 10.1364/OE.26.00A487.
- [17] S. Manzoor *et al.*, “Improved light management in planar silicon and perovskite solar cells using PDMS scattering layer,” *Sol. Energy Mater. Sol. Cells*, vol. 173, 2017, doi: 10.1016/j.solmat.2017.06.020.
- [18] M. H. Elshorbagy, K. Abdelhady, H. Kamal, and J. Alda, “Broadband anti-reflection coating using dielectric Si₃N₄ nanostructures. Application to amorphous-Si-H solar cells,” *Opt. Commun.*, vol. 390, pp. 130–136, 2017, doi: 10.1016/j.optcom.2016.12.062.
- [19] J. Yang *et al.*, “Plasmonic polymer tandem solar cell,” *ACS Nano*, vol. 5, no. 8, pp. 6210–6217, Aug. 2011, doi: 10.1021/NN202144B/SUPPL_FILE/NN202144B_SI_001.PDF.
- [20] E. Tiguntseva *et al.*, “Resonant silicon nanoparticles for enhancement of light absorption and photoluminescence from hybrid perovskite films and metasurfaces,” *Nanoscale*, vol. 9, no. 34, pp. 12486–12493, Sep. 2017, doi: 10.1039/c7nr01631j.
- [21] A. Mellor, N. P. Hylton, S. A. Maier, and N. Ekins-Daukes, “Interstitial light-trapping design for multi-junction solar cells,” *Sol. Energy Mater. Sol. Cells*, vol. 159, pp. 212–218, Jan. 2017, doi: 10.1016/j.solmat.2016.09.005.
- [22] M. H. Elshorbagy, B. García-Cámara, E. López-Fraguas, and R. Vergaz, “Efficient light management in a monolithic tandem perovskite/silicon solar cell by using a hybrid metasurface,” *Nanomaterials*, vol. 9, no. 5, May 2019, doi: 10.3390/nano9050791.
- [23] D. Chen *et al.*, “Nanophotonic Light Management for Perovskite-Silicon Tandem Solar Cells,” *arXiv*, Jan. 2018, doi: 10.1117/1.JPE.8.022601.
- [24] A. B. Numan and M. S. Sharawi, “Extraction of Material Parameters for Metamaterials Using a Full-Wave Simulator [Education Column],” *IEEE Antennas Propag. Mag.*, vol. 55,

no. 5, pp. 202–211, 2013, doi: 10.1109/MAP.2013.6735515.

- [25] B. Hamza, B. Abdelkader, S. Meskine, M. Hadjab, M. Ziane, and A. Zaoui, “First principles investigation of optoelectronic properties of ZnXP₂ (X = Si, Ge) lattice matched with silicon for tandem solar cells applications using the mBJ exchange potential,” *Opt. - Int. J. Light Electron Opt.*, vol. Volume 159, 2018, doi: 10.1016/j.ijleo.2018.01.079.
- [26] U.-G. Jong, C.-J. Yu, Y.-H. Kye, Y.-G. Choe, W. Hao, and S. Li, “First-Principles Study on Structural, Electronic, and Optical Properties of Inorganic Ge-Based Halide Perovskites,” *Inorg. Chem.*, vol. 58, no. 7, pp. 4134–4140, Apr. 2019, doi: 10.1021/acs.inorgchem.8b03095.
- [27] J. Even *et al.*, “Density Functional Theory Simulations of Semiconductors for Photovoltaic Applications: Hybrid Organic-Inorganic Perovskites and III/V Heterostructures,” *Int. J. Photoenergy*, vol. 2014, p. 649408, 2014, doi: 10.1155/2014/649408.
- [28] U. Neupane, B. Bahrami, M. Biesecker, M. F. Baroughi, and Q. Qiao, “Kinetic Monte Carlo modeling on organic solar cells: Domain size, donor-acceptor ratio and thickness,” *Nano Energy*, vol. 35, pp. 128–137, 2017, doi: <https://doi.org/10.1016/j.nanoen.2017.03.041>.
- [29] D. Chen and P. Manley, “Nanophotonic light management for perovskite–silicon tandem solar cells,” *J. Photonics Energy*, vol. 8, no. 02, p. 1, 2018, doi: 10.1117/1.jpe.8.022601.
- [30] M. Mousa, F. Z. Amer, R. I. Mubarak, and A. Saeed, “Simulation of optimized high-current tandem solar-cells with efficiency beyond 41%,” *IEEE Access*, vol. 9, pp. 49724–49737, 2021, doi: 10.1109/ACCESS.2021.3069281.
- [31] R. I. Rabady and H. Manasreh, “Thicknesses optimization of two- and three-junction photovoltaic cells with matched currents and matched lattice constants,” *Sol. Energy*, vol. 158, no. May, pp. 20–27, 2017, doi: 10.1016/j.solener.2017.09.016.
- [32] S. Sharma, K. Jain, and A. Sharma, “Solar Cells: In Research and Applications—A Review,” *Mater. Sci. Appl.*, vol. 06, pp. 1145–1155, 2015, doi: 10.4236/msa.2015.612113.
- [33] H. Ullah, A. Khan, A. Ullah, I. Ullah, and M. Noman, “Plasmonic perfect absorber for solar cell applications,” 2016, pp. 1–5. doi: 10.1109/ICET.2016.7813268.
- [34] N. I. Landy, S. Sajuyigbe, J. J. Mock, D. R. Smith, and W. Padilla, “Perfect Metamaterial Absorber,” *Phys. Rev. Lett.*, vol. 100, p. 207402, 2008, doi: 10.1103/PhysRevLett.100.207402.
- [35] S. K. Patel, K. Shah, and Y. Kosta, “Frequency reconfigurable and high gain metamaterial microstrip radiating structure,” *Waves in Random and Complex Media*, vol. 29, 2018, doi: 10.1080/17455030.2018.1452309.
- [36] H.-L. Huang, H. Xia, Z.-B. Guo, D. Xie, and H.-J. Li, “Design of Broadband Metamaterial Absorbers for Permittivity Sensitivity and Solar Cell Application *,” *Chinese Phys. Lett.*,

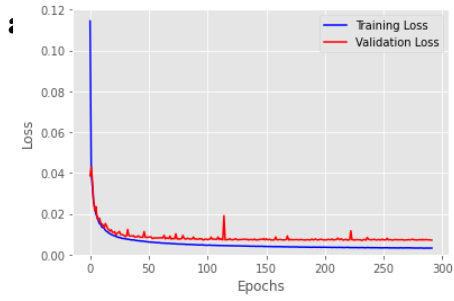
- vol. 34, p. 117801, 2017, doi: 10.1088/0256-307X/34/11/117801.
- [37] W. Xin, Z. Binzhen, W. Wanjun, W. Junlin, and D. Junping, “Design and Characterization of an Ultra-broadband Metamaterial Microwave Absorber,” *IEEE Photonics J.*, vol. PP, p. 1, 2017, doi: 10.1109/JPHOT.2017.2700056.
- [38] K. Matsumori and R. Fujimura, “Broadband light absorption of an Al semishell-MIM nanostructure in the UV to near-infrared regions,” *Opt. Lett.*, vol. 43, pp. 2981–2984, 2018, doi: 10.1364/OL.43.002981.
- [39] C. Cao and Y. Cheng, “A broadband plasmonic light absorber based on a tungsten meandering-resonator in visible region,” *Appl. Phys. A*, vol. 125, 2019, doi: 10.1007/s00339-018-2310-1.
- [40] M. I. Hossain *et al.*, “Non-resonant metal-oxide metasurfaces for efficient perovskite solar cells,” *Sol. Energy*, vol. 198, no. August 2019, pp. 570–577, 2020, doi: 10.1016/j.solener.2020.01.082.
- [41] V. Neder, D. Zhang, S. Veenstra, and A. Polman, “Four-terminal perovskite/silicon tandem solar cell with integrated Mie-resonant spectral splitter metagrating,” *arXiv*, pp. 1–15, 2020.
- [42] C. Wang and Z. Zhang, “Broadband optical absorption enhancement in hybrid organic-inorganic perovskite metasurfaces,” *AIP Adv.*, vol. 11, no. 2, 2021, doi: 10.1063/5.0037367.
- [43] D. H. Hubel and T. N. Wiesel, “Receptive fields of single neurones in the cat’s striate cortex,” *J. Physiol.*, vol. 148, no. 3, pp. 574–591, Oct. 1959, doi: 10.1113/JPHYSIOL.1959.SP006308.
- [44] K. Fukushima, “Neocognitron: A hierarchical neural network capable of visual pattern recognition,” *Neural Networks*, vol. 1, no. 2, pp. 119–130, Jan. 1988, doi: 10.1016/0893-6080(88)90014-7.
- [45] Y. LeCun *et al.*, “Backpropagation Applied to Handwritten Zip Code Recognition,” *Neural Comput.*, vol. 1, no. 4, pp. 541–551, Dec. 1989, doi: 10.1162/NECO.1989.1.4.541.
- [46] O. Russakovsky *et al.*, “ImageNet Large Scale Visual Recognition Challenge,” *Int. J. Comput. Vis.*, vol. 115, no. 3, pp. 211–252, Dec. 2015, doi: 10.1007/S11263-015-0816-Y/FIGURES/16.
- [47] A. Krizhevsky, I. Sutskever, and G. E. Hinton, “ImageNet classification with deep convolutional neural networks,” *Commun. ACM*, vol. 60, no. 6, pp. 84–90, May 2017, doi: 10.1145/3065386.
- [48] K. Simonyan and A. Zisserman, “Very Deep Convolutional Networks for Large-Scale Image Recognition,” *arXiv 1409.1556*, 2014.
- [49] C. Szegedy *et al.*, “Going deeper with convolutions,” in *2015 IEEE Conference on*

- Computer Vision and Pattern Recognition (CVPR)*, 2015, pp. 1–9. doi: 10.1109/CVPR.2015.7298594.
- [50] K. He, X. Zhang, S. Ren, and J. Sun, “Deep Residual Learning for Image Recognition,” in *2016 IEEE Conference on Computer Vision and Pattern Recognition (CVPR)*, 2016, pp. 770–778. doi: 10.1109/CVPR.2016.90.
- [51] K. Jäger, L. Korte, B. Rech, and S. Albrecht, “Numerical optical optimization of monolithic planar perovskite-silicon tandem solar cells with regular and inverted device architectures,” *Opt. Express*, vol. 25, no. 12, pp. A473–A482, Jun. 2017, doi: 10.1364/OE.25.00A473.
- [52] J. K. Chaudhary, J. Liu, J. P. Skön, Y. W. Chen, R. K. Kanth, and J. Heikkonen, *Optimization of Silicon Tandem Solar Cells Using Artificial Neural Networks*, vol. 11927 LNAI, no. December. Springer International Publishing, 2019. doi: 10.1007/978-3-030-34885-4_30.
- [53] C. Yi, Y. Wu, Y. Gao, and Q. Du, “Tandem solar cells efficiency prediction and optimization via deep learning,” *Phys. Chem. Chem. Phys.*, vol. 23, no. 4, pp. 2991–2998, 2021, doi: 10.1039/d0cp05882c.
- [54] H. Q. Tan, X. Zhao, A. Jiao, E. Birgersson, and H. Xue, “Optimizing bifacial all-perovskite tandem solar cell: How to balance light absorption and recombination,” *Sol. Energy*, vol. 231, pp. 1092–1106, 2022, doi: <https://doi.org/10.1016/j.solener.2021.12.040>.
- [55] W. A. Saidi, W. Shadid, and I. E. Castelli, “Machine-learning structural and electronic properties of metal halide perovskites using a hierarchical convolutional neural network,” *npj Comput. Mater.*, vol. 6, no. 1, pp. 1–7, 2020, doi: 10.1038/s41524-020-0307-8.
- [56] K. Jäger, J. Sutter, M. Hammerschmidt, P. I. Schneider, and C. Becker, “Prospects of light management in perovskite/silicon tandem solar cells,” *Nanophotonics*, vol. 10, no. 8, pp. 1991–2000, 2021, doi: 10.1515/nanoph-2020-0674.
- [57] M. H. Elshorbagy, B. García-Cámara, E. López-Fraguas, and R. Vergaz, “Efficient Light Management in a Monolithic Tandem Perovskite/Silicon Solar Cell by Using a Hybrid Metasurface,” *Nanomater. (Basel, Switzerland)*, vol. 9, no. 5, May 2019, doi: 10.3390/NANO9050791.
- [58] C. Yeung, J. M. Tsai, B. King, Y. Kawagoe, D. Ho, and A. Raman, “Elucidating the physics of nanophotonic structures through explainable machine learning algorithms,” *Opt. InfoBase Conf. Pap.*, pp. 1–17, 2020, doi: 10.1364/FIO.2020.FM2A.2.
- [59] “Calculating absorbed optical power - Simple method - Ansys Optics.” <https://optics.ansys.com/hc/en-us/articles/360034915673-Calculating-absorbed-optical-power-Simple-method> (accessed Feb. 11, 2023).
- [60] A. D. C. A. Ishteev, K. Konstantinova, G. Ermolaev, D. Kiselev, D. Muratov, M. Voronova, T. Ilina, P. Lagov, O. Uvarov, Y. Pavlov, M. Letovaltseva, A. Arsenin, V. Volkov, S.

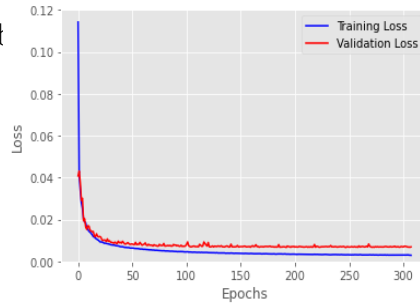
- Didenko, D. Saranin, “Investigation of structural and optical properties of MAPbBr₃ monocrystals under fast electron irradiation,” *J. Mater. Chem. C*, vol. 10, pp. 5821–5828, 2022.
- [61] S. Li, Y. L. Cao, W. H. Li, and Z. S. Bo, “A brief review of hole transporting materials commonly used in perovskite solar cells,” *Rare Met.*, vol. 40, no. 10, pp. 2712–2729, 2021, doi: 10.1007/s12598-020-01691-z.
- [62] S. S. I. Bodurov, I. Vlaeva, A. Viraneva, T. Yovcheva, “Modified design of a laser refractometer,” *Nanosci. Nanotechnol.*, vol. 16, pp. 311–33, 2016.
- [63] E. Trushin, M. Betzinger, S. Blügel, and A. Görling, “Band gaps, ionization potentials, and electron affinities of periodic electron systems via the adiabatic-connection fluctuation-dissipation theorem,” *Phys. Rev. B*, vol. 94, p. 75123, 2016.
- [64] K. B. Sundaram and A. Khan, “Work function determination of zinc oxide films,” *J. Vac. Sci. Technol. A*, vol. 15, no. 2, pp. 428–430, 1997, doi: 10.1116/1.580502.
- [65] B. Mahapatra, R. V. Krishna, Laxmi, and P. K. Patel, “Design and optimization of CuSCN/CH₃NH₃PbI₃/TiO₂ perovskite solar cell for efficient performance,” *Opt. Commun.*, vol. 504, p. 127496, 2022, doi: <https://doi.org/10.1016/j.optcom.2021.127496>.
- [66] X. Liu *et al.*, “Simulation of p-type c-Si solar cells with metal oxides as carrier-selective contacts,” *Sol. Energy*, vol. 240, pp. 84–89, 2022, doi: <https://doi.org/10.1016/j.solener.2022.05.030>.
- [67] F. Wei, L. Yao, F. Lan, G. Li, and L. Liu, “Tandem polymer solar cells: Simulation and optimization through a multiscale scheme,” *Beilstein J. Nanotechnol.*, vol. 8, no. 1, pp. 123–133, 2017, doi: 10.3762/bjnano.8.13.
- [68] Colin David Bailie, “Polycrystalline Tandem Photovoltaics,” *Dr. Thesis, Department Mater. Sci. Eng. Stanford Univ.*, 2015.

Appendix

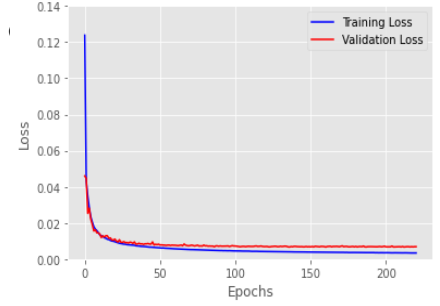
Training and Validation Losses of CNN Model 1-8



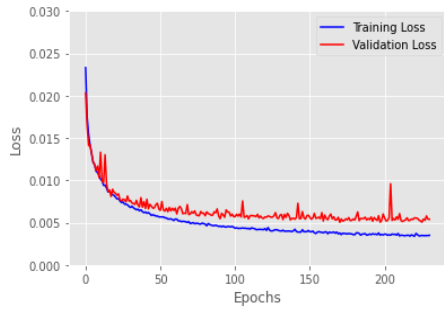
Model 1



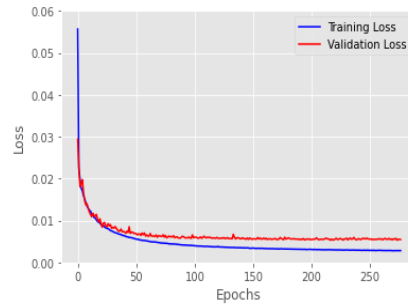
Model 2



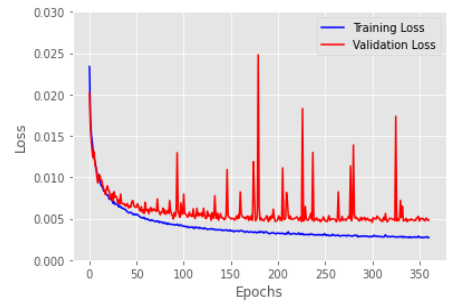
Model 3



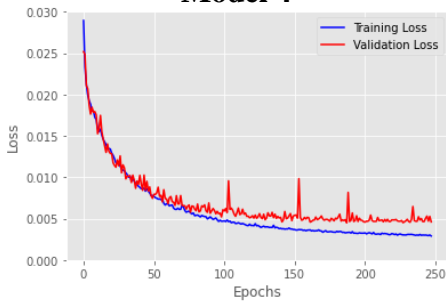
Model 4



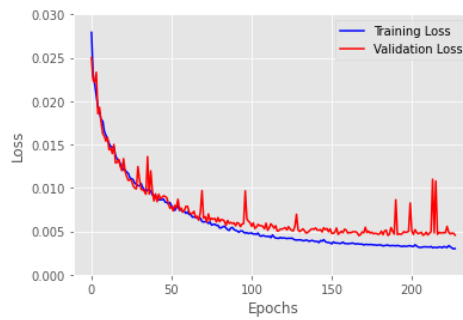
Model 5



Model 6



Model 7



Model 8